

Nucleon isovector couplings from $N_f = 2$ lattice QCD

Gunnar S. Bali,^{1,2,*} Sara Collins,^{1,†} Benjamin Gläsel,¹ Meinulf Göckeler,¹ Johannes Najjar,¹ Rudolf H. Rödl,¹ Andreas Schäfer,¹ Rainer W. Schiel,¹ Wolfgang Söldner,¹ André Sternbeck^{3,1}
(RQCD Collaboration)

¹*Institut für Theoretische Physik, Universität Regensburg, 93040 Regensburg, Germany*

²*Tata Institute of Fundamental Research, Homi Bhabha Road, Mumbai 400005, India*

³*Theoretisch-Physikalisches Institut, Friedrich-Schiller-Universität Jena,*

Max-Wien-Platz 1, 07743 Jena, Germany

(Received 23 December 2014; published 5 March 2015)

We compute the axial, scalar, tensor and pseudoscalar isovector couplings of the nucleon as well as the induced tensor and pseudoscalar charges in lattice simulations with $N_f = 2$ mass-degenerate non-perturbatively improved Wilson-Sheikholeslami-Wohlert fermions. The simulations are carried out down to a pion mass of 150 MeV and linear spatial lattice extents of up to 4.6 fm at three different lattice spacings ranging from approximately 0.08 fm to 0.06 fm. Possible excited state contamination is carefully investigated and finite volume effects are studied. The couplings, determined at these lattice spacings, are extrapolated to the physical pion mass. In this limit we find agreement with experimental results, where these exist, with the exception of the magnetic moment. A proper continuum limit could not be performed, due to our limited range of lattice constants, but no significant lattice spacing dependence is detected. Upper limits on discretization effects are estimated and these dominate the error budget.

DOI: 10.1103/PhysRevD.91.054501

PACS numbers: 12.38.Gc, 13.60.Fz, 13.75.-n, 14.20.Dh

I. INTRODUCTION

The electron spectrum measured in nuclear β decays led to Pauli's postulate of an electrically neutral, almost massless particle in his famous letter presented to a meeting of nuclear physicists in 1930 (reprinted and translated in Ref. [1]). The existence of this particle was confirmed with the discovery of the electron antineutrino some 25 years later [2]. The axial coupling (or charge) of the nucleon $g_A = 1.2723(23)g_V$ [3] associated with the β decay of the neutron into a proton is experimentally well determined (see, e.g., Ref. [4]) and a parameter of fundamental importance for the structure of baryons. Also the induced tensor charge $\tilde{g}_T \approx \mu_p - \mu_n - 1 = 3.7058901(5)$ [3] is well known as it quantifies the difference between the anomalous magnetic moments of the proton and the neutron while the vector charge $g_V = 1$ is fixed due to baryon number conservation.¹ Computing these quantities provides a nontrivial cross-check of lattice predictions of similar observables.

Little is known about charges related to flavor changing processes in any other channels since these do not feature in tree-level standard model interactions. However, new physics processes analogous to the standard model nucleon

β -decay or neutrino capture may depend on such parameters, see, e.g., Refs. [6–8]. This is, in particular, also relevant with respect to dark matter searches. Only the pseudoscalar charges are, to some extent, constrained through the effective field theory description of low energy scattering processes $n + \pi^+ \rightarrow p + \pi^0$, see Ref. [9] and references therein, as well as by the current algebra relations discussed below. The charges g_T and g_S can at present only be determined through lattice simulation.

In this article we compute the isovector nucleon couplings g_A, g_V, g_S, g_T, g_P and the induced charges \tilde{g}_T and g_P^* , simulating $N_f = 2$ QCD down to a nearly physical quark mass. For calculations of isovector charges one can rely on standard methods. In particular, quark-line disconnected contributions to correlation functions cancel in the isospin symmetric case which we realize here, i.e. we neglect the mass difference between and the electric charges of up and down quarks.

We extract the couplings from the following form factors at $q^2 = 0$, where—in contrast to the remainder of this article—we employ Minkowski spacetime conventions:

$$\langle p | \bar{u} d | n \rangle = g_S(q^2) \bar{u}_p(\mathbf{p}_f) u_n(\mathbf{p}_i), \quad (1)$$

$$\langle p | \bar{u} \gamma_5 d | n \rangle = g_P(q^2) \bar{u}_p(\mathbf{p}_f) \gamma_5 u_n(\mathbf{p}_i), \quad (2)$$

$$\langle p | \bar{u} \gamma_\mu d | n \rangle = \bar{u}_p(\mathbf{p}_f) \left[g_V(q^2) \gamma_\mu + \frac{\tilde{g}_T(q^2)}{2m_N} i \sigma_{\mu\nu} q^\nu \right] u_n(\mathbf{p}_i), \quad (3)$$

*gunnar.bali@ur.de

†sara.collins@ur.de

¹In the isovector channel that we consider here there will be corrections to $g_V = 1$ to second order in the isospin breaking parameter [5], however, we assume isospin symmetry.

$$\langle p|\bar{u}\gamma_\mu\gamma_5d|n\rangle = \bar{u}_p(\mathbf{p}_f)\left[g_A(q^2)\gamma_\mu + \frac{\tilde{g}_P(q^2)}{2m_N}q_\mu\right]\gamma_5u_n(\mathbf{p}_i), \quad (4)$$

$$\langle p|\bar{u}\sigma_{\mu\nu}d|n\rangle = g_T(q^2)\bar{u}_p(\mathbf{p}_f)\sigma_{\mu\nu}u_n(\mathbf{p}_i), \quad (5)$$

where $\sigma_{\mu\nu} = \frac{i}{2}[\gamma_\mu, \gamma_\nu]$. Above, we have assumed isospin symmetry [6,10]. The proton and neutron states $|p\rangle$ and $|n\rangle$ carry four-momenta p_f and p_i , respectively. u_p and u_n denote the proton and neutron spinors, m_N the nucleon mass and the momentum transfer is $q_0 = \sqrt{m_N^2 + \mathbf{p}_f^2 - \sqrt{m_N^2 + \mathbf{p}_i^2}}$, $\mathbf{q} = \mathbf{p}_f - \mathbf{p}_i$. The virtuality is given as $Q^2 = -q^2 \geq 0$. In the isospin symmetric limit the identity $g_V \equiv g_V(0) = 1$ holds for the isovector vector charge [5] (and therefore $\lambda \equiv g_A/g_V = g_A$) since

$$\begin{aligned} \langle p|\bar{u}\Gamma d|n\rangle &= \langle p|(\bar{u}\Gamma u - \bar{d}\Gamma d)|p\rangle = \langle n|(\bar{d}\Gamma d - \bar{u}\Gamma u)|n\rangle \\ &= \langle p|\left(\frac{2}{3}\bar{u}\Gamma u - \frac{1}{3}\bar{d}\Gamma d\right)|p\rangle \\ &\quad - \langle n|\left(\frac{2}{3}\bar{u}\Gamma u - \frac{1}{3}\bar{d}\Gamma d\right)|n\rangle. \end{aligned} \quad (6)$$

Here we construct the above matrix elements as $\langle p|(\bar{u}\Gamma u - \bar{d}\Gamma d)|p\rangle$, in which case the function $g_V(q^2)$ is also known as the Dirac form factor $F_1^p(q^2) - F_1^n(q^2)$ and $\tilde{g}_T(q^2)$ as the Pauli form factor $F_2^p(q^2) - F_2^n(q^2)$. Note that $\tilde{g}_T = \kappa_{u-d} \approx \kappa_p - \kappa_n$ determines the difference between the anomalous magnetic moments of the proton and the neutron ($\mu_p = 1 + \kappa_p$, $\mu_n = \kappa_n$), $g_T = \langle 1 \rangle_{\delta u - \delta d}$ is the first Mellin moment of the isovector transversity distribution function and $g_A = \langle 1 \rangle_{\Delta u - \Delta d}$ that of the spin distribution function.

With the exceptions of g_P^* (defined below) and \tilde{g}_T which require extrapolations in q^2 , all couplings can directly be accessed in the forward limit: $g_S = g_S(0)$, $g_V = g_V(0)$, $g_A = g_A(0)$ and $g_T = g_T(0)$. The determination of the pseudoscalar, axial and tensor couplings requires polarized nucleon states. We remark that g_V , g_A , \tilde{g}_T and g_P^* are scale independent while g_T , g_P and g_S carry anomalous dimensions. In these cases our results will refer to the $\overline{\text{MS}}$ scheme at a renormalization scale $\mu = 2$ GeV. Also note that the couplings g_P and g_S share the negative anomalous dimension of the quark mass m_{ud} so that combinations $g_S m_{ud}$ or $g_P m_{ud}$ are scale independent.

The conservation of the isovector axial current (PCAC) implies the relation [11–13]

$$m_{ud}g_P(q^2) = m_N g_A(q^2) + \frac{q^2}{4m_N} \tilde{g}_P(q^2). \quad (7)$$

The right-hand side of this expression can be extrapolated to $q^2 = 0$, giving

$$m_{ud}g_P = m_N g_A = F_\pi g_{\pi NN} [1 + \mathcal{O}(m_\pi^2)], \quad (8)$$

where the second equality is the Goldberger-Treiman relation [14], $F_\pi \approx 92$ MeV denotes the pion decay constant and $g_{\pi NN}$ the pion-nucleon-nucleon coupling. The chiral perturbation theory corrections to this relation due to the nonvanishing pion mass are discussed in Refs. [9,15–17]. We will use the first equality in Eq. (8) to determine g_P .

Equation (7) implies $\tilde{g}_P(q^2) = -4m_N^2 g_A(q^2)/q^2$ at zero quark mass, which suggests $\tilde{g}_P(q^2)$ is governed by a pion pole at small q^2 and m_π ,

$$\tilde{g}_P(q^2) = \frac{4c_N^2}{m_\pi^2 - q^2} g_A(q^2) + \dots, \quad (9)$$

where the ellipses refer to corrections that are regular at $q^2 < m_\pi^2$ or, equivalently, at $Q^2 > -m_\pi^2$ and c_N approaches the nucleon mass as $m_\pi \rightarrow 0$. Finally, the induced pseudoscalar coupling

$$g_P^* = \frac{m_\mu}{m_N} \tilde{g}_P(-0.88m_\mu^2) \quad (10)$$

quantifies the muon capture process [14,18,19] $\mu^- p \rightarrow \nu_\mu n$, where the scale $Q^2 = 0.88m_\mu^2$ corresponds to the kinematic threshold and m_μ denotes the muon mass.

Responding to the phenomenological demand, several groups have recently determined g_A [20–29], g_T [30,31], g_S and g_T [32], g_A and the induced pseudoscalar form factor [33–36], g_A , g_P and g_P^* [37,38] or g_A , g_S and g_T [39,40] or the related form factors in lattice simulations. g_V and \tilde{g}_T are frequently determined in calculations of the electromagnetic form factors [28,33,35,38,39,41–47], also see Refs. [48–52] for recent reviews. Here we compute the complete set of isovector couplings down to a nearly physical quark mass. We note that a preliminary analysis on g_A , g_S and g_T using a subset of our ensembles appeared in Ref. [53].

This article is organized as follows. In Sec. II we introduce our gauge ensembles and the analysis methods used. Then in Sec. III we check the nonperturbative renormalization by computing g_V and also present results on g_A , which serves as a benchmark quantity. In the latter case we find significant finite size effects. These are addressed in Sec. IV, where we also investigate the volume dependence of the pion mass m_π and the pion decay constant F_π . In Sec. V we present results on the remaining couplings g_S , g_T , \tilde{g}_T , g_P , g_P^* and $g_{\pi NN}$. We summarize our findings in Sec. VI.

II. SIMULATION DETAILS

A. Lattice setup

We analyze several gauge ensembles that were generated employing $N_f = 2$ nonperturbatively improved

TABLE I. Details of the ensembles used in this analysis. $N(n)$ indicates the number of configurations N and the number of measurements per configuration n . N_{sm} refers to the number of Wuppertal smearing iterations and t_f to the sink-source time differences realized. For small t_f values the numbers of measurements per configuration n were reduced (indicated in brackets after the respective t_f/a entries). Note that the pion and nucleon masses displayed were obtained on the respective ensembles and are not extrapolated to their infinite volume limits. The two errors of am_π and am_N are statistical and from varying the fit range, respectively. The error of the pion mass in physical units includes both sources of uncertainty.

Ensemble	β	a [fm]	κ	V	am_π	m_π [GeV]	am_N	Lm_π	$N(n)$	N_{sm}	t_f/a
I	5.20	0.081	0.13596	$32^3 \times 64$	0.11516(73)(11)	0.2795(18)	0.4480(31)(06)	3.69	1986(4)	300	13
II	5.29	0.071	0.13620	$24^3 \times 48$	0.15449(69)(26)	0.4264(20)	0.4641(53)(05)	3.71	1999(2)	300	15
III			0.13620	$32^3 \times 64$	0.15298(43)(16)	0.4222(13)	0.4486(22)(20)	4.90	1998(2)	300	15,17
IV			0.13632	$32^3 \times 64$	0.10675(51)(08)	0.2946(14)	0.3855(39)(23)	3.42	2023(2)	400	7(1),9(1),11(1), 13,15,17
V				$40^3 \times 64$	0.10465(37)(08)	0.2888(11)	0.3881(32)(12)	4.19	2025(2)	400	15
VI				$64^3 \times 64$	0.10487(24)(04)	0.2895(07)	0.3856(19)(05)	6.71	1232(2)	400	15
VII			0.13640	$48^3 \times 64$	0.05786(51)(21)	0.1597(15)	0.3484(69)(21)	2.78	3442(2)	400	15
VIII				$64^3 \times 64$	0.05425(40)(28)	0.1497(13)	0.3398(61)(18)	3.47	1593(3)	400	9(1), 12(2), 15
IX	5.40	0.060	0.13640	$32^3 \times 64$	0.15020(53)(06)	0.4897(17)	0.3962(33)(06)	4.81	1123(2)	400	17
X			0.13647	$32^3 \times 64$	0.13073(55)(28)	0.4262(20)	0.3836(29)(14)	4.18	1999(2)	450	17
XI			0.13660	$48^3 \times 64$	0.07959(25)(09)	0.2595(09)	0.3070(26)(43)	3.82	2177(2)	600	17

Sheikholeslami-Wohlert (NPI Wilson-clover) fermions, using the Wilson gauge action by the RQCD and QCDSF collaborations. Three lattice spacings were realized, corresponding to $a \approx 0.081$ fm ($\beta = 5.20$), $a \approx 0.071$ fm ($\beta = 5.29$) and $a \approx 0.060$ fm ($\beta = 5.40$), where the lattice spacing was set using the value $r_0 = 0.5$ fm at vanishing quark mass, obtained by extrapolating the nucleon mass to the physical point [54]. This is consistent with determinations from the Ω baryon mass [55] or the kaon decay constant [56]. With the exceptions of \tilde{g}_T and g_p^* we implement full order- a improvement such that our leading lattice spacing effects are of $\mathcal{O}(a^2)$. We vary a^2 by a

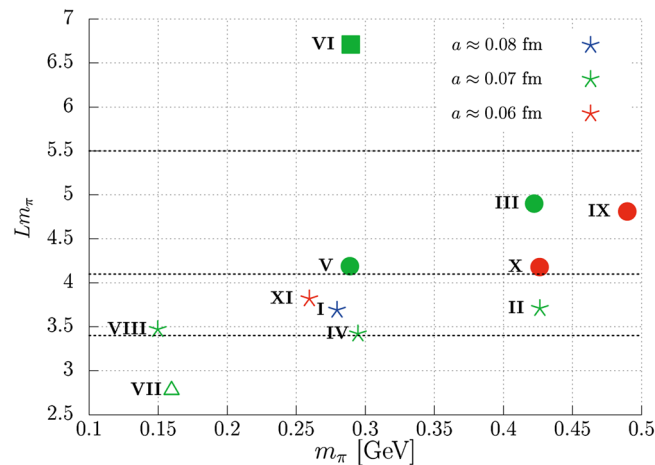


FIG. 1 (color online). Overview of the ensembles listed in Table I. Colors encode the lattice spacings and symbols the lattice extents. The color and symbol labeling defined here will be used throughout in Secs. III–V. The horizontal lines separate different volume ranges.

factor of about 1.8. However, not all volumes and quark masses are realized at all three lattice spacings.

The analyzed ensembles are listed in Table I and illustrated in Fig. 1, see also Ref. [57]. Our largest pion mass (ensemble IX) corresponds to $m_\pi \approx 490$ MeV. Around $m_\pi \approx 425$ MeV two lattice spacings and two different spatial lattice extents L are available. Within the window $260 \text{ MeV} \lesssim m_\pi < 290 \text{ MeV}$ we cover three lattice spacings and several volumes up to $Lm_\pi \approx 6.7$. The smallest mass $m_\pi \approx 150$ MeV was simulated at only one lattice spacing ($a \approx 0.071$) but for two volumes ($Lm_\pi \approx 2.8$ and 3.5). In Table I we also list the nucleon masses in lattice units. Note that, with the exception of ensemble IX, all masses agree within one to two standard deviations with our previous analysis [54], where in some cases we employed an inferior quark smearing.

To improve the overlap of our nucleon interpolators with the physical ground state, we follow Ref. [58] and employ Wuppertal (Gauss) smearing [59] of the quark fields

$$\phi_x^{(n)} = \frac{1}{1 + 6\delta} \left(\phi_x^{(n-1)} + \delta \sum_{j=\pm 1}^{\pm 3} U_{x,j} \phi_{x+aj}^{(n-1)} \right), \quad (11)$$

where we replace the spatial links $U_{x,j}$ by APE-smearing [60] gauge links

$$U_{x,i}^{(n)} = P_{\text{SU}(3)} \left(\alpha U_{x,i}^{(n-1)} + \sum_{|j| \neq i} U_{x,j}^{(n-1)} U_{x+aj,i}^{(n-1)} U_{x+ai,j}^{(n-1)\dagger} \right) \quad (12)$$

with $i \in \{1, 2, 3\}$, $j \in \{\pm 1, \pm 2, \pm 3\}$. $P_{\text{SU}(3)}$ denotes a projection into the SU(3) group and the sum is over the

four spatial ‘‘staples,’’ surrounding $U_{x,i}$. We employ 25 such gauge covariant smearing iterations and use the weight factor $\alpha = 2.5$. Within the Wuppertal smearing we set $\delta = 0.25$ and adjust the number of iterations to optimize the quality of the effective mass plateaus of smeared-smeared nucleon two-point functions.

We label the nucleon source time as $t_i = 0$ and the sink time as t_f . The currents are inserted at times $t \in [0, t_f]$ and the relevant matrix elements can be extracted from data within the range $t \in [\delta t, t_f - \delta t]$ where $\delta t \geq 2a$, due to the clover term in the action that couples adjacent time slices. Using the sequential source method² [64], all values of t can be realized, essentially without overhead. However, each t_f value requires additional computations of sequential propagators, adding to the cost. On some of our ensembles we vary this distance too, since this may be necessary to parametrize and eliminate excited state contributions. The t_f values used, the numbers of gauge configurations N and measurements per configuration n are also included in Table I. The statistical noise decreases with smaller Euclidean time distances between source and sink, which means we can reduce the number of three-point function measurements in some cases (indicated in brackets after the respective t_f/a entries).

Naively, one would expect the optimal number of smearing iterations N_{sm} to somewhat increase with decreasing quark mass and, at a fixed mass, to scale with $1/a^2$, maintaining a smearing radius that is constant in physical units. As can be read off from the table, we approximately follow this rule. In Fig. 2 we compare our effective nucleon masses

$$m_N(t_f + a/2) = a^{-1} \ln \left[\frac{C_{2\text{pt}}(t_f)}{C_{2\text{pt}}(t_f + a)} \right] \quad (13)$$

in physical units between ensembles III and X as well as between ensembles I, IV and V, see Fig. 1. These two groups of ensembles correspond to similar pion masses but differ in terms of the lattice spacing. Using our optimized smearing functions in the construction of the nucleon interpolators, we do not detect any significant lattice spacing dependence of the shapes of the resulting effective mass curves. In Fig. 3 the same comparison is made for smeared-smeared pion effective masses. Again, the shapes within each group of ensembles are very similar while obviously in this case we can resolve the small differences between the lower pion masses.

Our nucleon sources were placed at different time slices and spatial positions from configuration to configuration to reduce autocorrelations. Remaining autocorrelations were accounted for by binning subsequent configurations within the jackknife error analysis and varying the bin sizes until

²We also explored stochastic methods [61], see also Refs. [62,63].

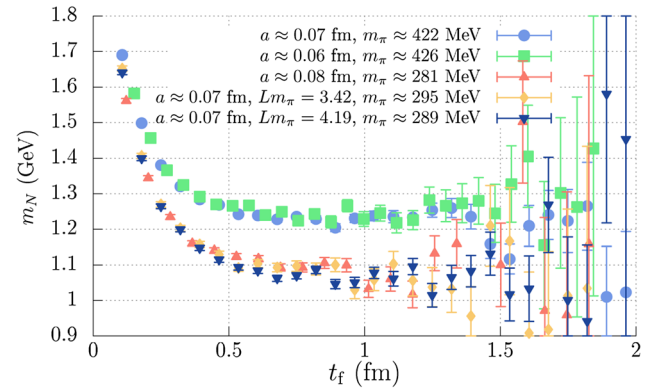


FIG. 2 (color online). Effective nucleon masses Eq. (13) for five of our ensembles, computed from smeared-smeared two-point functions $C_{2\text{pt}}(t_f)$.

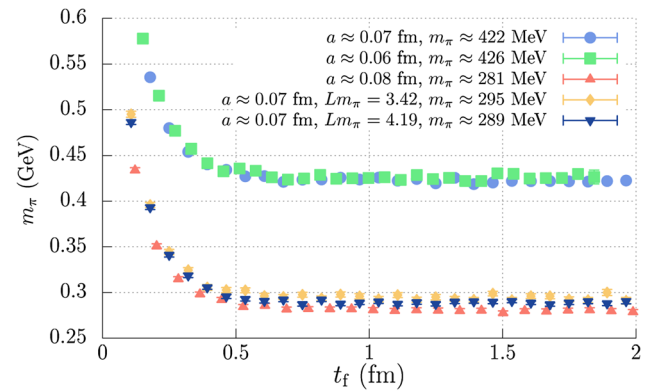


FIG. 3 (color online). The same as Fig. 2 for the pion effective mass.

they were bigger than four times the respective estimated integrated autocorrelation times.

Recently, many groups investigated the issue of excited state contamination of ground state signals of three-point functions and, indeed, by applying a more careful analysis, varying t_f [21–24,27,28,32,36,37,39,40,57,65], using a variational approach [25] and/or by optimizing the ground state overlap of the nucleon interpolator [24,57] significant effects were detected in many matrix elements. Hence, for three of our ensembles, covering the pion masses 150 MeV (VIII), 290 MeV (IV) and 425 MeV (III), we vary the source-sink distance t_f in addition to the position of the current t , see Table I. Based on these results and our observation of very similar shapes as a function of time of the effective masses computed from our nucleon two-point functions (see Fig. 2), for the remaining ensembles we fix $t_f \gtrsim 1$ fm.

B. Excited state analysis

The spectral decompositions for two- and three-point functions read

$$C_{2\text{pt}}(t_f) = A_0 e^{-m_N t_f} (1 + A_1 e^{-\Delta m_N t_f} + \dots), \quad (14)$$

$$C_{3\text{pt}}(t, t_f) = A_0 e^{-m_N t_f} [B_0 + B_{01} e^{-\Delta m_N t_f/2} \cosh(\Delta m_N t) + B_1 e^{-\Delta m_N t_f} + \dots], \quad (15)$$

where $\Delta m_N = m_{N'} - m_N$ denotes the mass gap between the nucleon ground state and its first excitation and the ellipses denote contributions from higher excited states. The coefficients A_0 , A_1 , B_0 , B_{01} and B_1 are real if the current is self-adjoint (or anti-self-adjoint) and the same interpolator (i.e. smearing) is used at the source and the sink. Above we assumed the temporal lattice extent to be much bigger than t_f which holds in our case.

For a current $J = \bar{u}\Gamma d$, a nucleon interpolator Φ , a nucleon state $|N\rangle$ (and first excitation $|N'\rangle$) and a vacuum state $|0\rangle$ the coefficients read³

$$A_0 = \frac{|\langle 0|\Phi|N\rangle|^2}{2m_N}, \quad A_1 = \frac{|\langle 0|\Phi|N'\rangle|^2}{2m_{N'}A_0}, \quad (16)$$

$$B_0 = \frac{\langle N|J|N\rangle}{2m_N}, \quad B_1 = A_1 \frac{\langle N'|J|N'\rangle}{2m_{N'}}, \quad (17)$$

$$B_{01} = \frac{2\text{Re}(\langle 0|\Phi|N\rangle\langle N|J|N'\rangle\langle N'|\Phi^\dagger|0\rangle)}{4m_N m_{N'} A_0}. \quad (18)$$

If for instance the transition matrix element $\langle N|J|N'\rangle$ and therefore B_{01} is small, this does not imply a small coefficient B_1 and vice versa. Hence it is essential to employ interpolators that minimize overlaps with higher excitations (i.e. $|\langle 0|\Phi|N'\rangle| \ll |\langle 0|\Phi|N\rangle|$ etc.) and to choose t_f sufficiently large.

For two-point functions excited states are suppressed by factors $e^{-\Delta m_N t_f}$ while in the three-point functions there exist contributions $\propto e^{-\Delta m_N t_f/2}$. If the ratio of the three-point function over the two-point function is constant upon varying t , this indicates a small $B_{01} e^{-\Delta m_N t_f/2}$ term, but still terms $(B_1 - A_1) e^{-\Delta m_N t_f}$ may be present that can only be isolated if t_f is varied as well. Up to such corrections the ratio reads

$$R(t, t_f) \equiv \frac{C_{3\text{pt}}(t, t_f)}{C_{2\text{pt}}(t_f)} = \frac{\langle N|J|N\rangle}{2m_N} + \dots, \quad (19)$$

where $\langle N|J|N\rangle$ is the matrix element of interest. Fitting this combination to a constant suffers from the obvious caveats described above.

³In our normalization we assume $|N'\rangle$ to be a one-particle state. However, the precise nature of $|N'\rangle$ does not have any impact on the discussion below nor does it affect any of the arguments or the analysis.

Recently, the summation method [64]

$$\frac{a}{t_f} \sum_{t=\delta t}^{t_f-\delta t} R(t, t_f) = \frac{\langle N|J|N\rangle}{2m_N} + c \frac{a}{t_f} + \mathcal{O}(e^{-\Delta m_N t_f}) \quad (20)$$

was advertised [65] as a more reliable alternative. In this case corrections $\propto e^{-\Delta m_N t_f/2}$ are removed, but a c/t_f term is introduced, adding a not necessarily small parameter c to the fit function. We refrain from quoting the corresponding results as direct fits to the known parametrization equations (14) and (15) are cleaner theoretically and utilize the whole functional dependence of the data on t and t_f . Since the summation method appears to be very popular, we discuss it in more detail in Sec. II C below.

First we discuss g_A . In Fig. 4 we display the ratio equation (19) of the renormalized (see Sec. III below) three-point over the two-point function obtained from ensemble VIII ($m_\pi \approx 150$ MeV) at $t_f = 15a \approx 1.07$ fm, $t_f = 12a$ and $t_f = 9a$. All three sets are compatible with constants, however, the $t_f = 9a \approx 0.64$ fm data are significantly lower than the two other sets. This indicates a small B_{01} coefficient in Eq. (15). The effect of $B_1 - A_1$ (or higher excitations) becomes visible at $t_f < 1$ fm. Whenever B_{01} could not be resolved, such as in the case shown in the figure, g_A was obtained from a fit of the plateau to a constant. Otherwise multiexponential fit equations (14) and (15) were performed, where B_1 was set to zero for the ensembles with only one t_f value. These multiexponential fits gave numbers compatible with those obtained by fitting the $t_f \gtrsim 1$ fm ratios to constants for g_A as well as for all the other couplings discussed in this article.

In all analyses presented in this article the fit ranges were selected based on the goodness of the correlated χ^2 values and the stability of the results upon reducing the fit range,

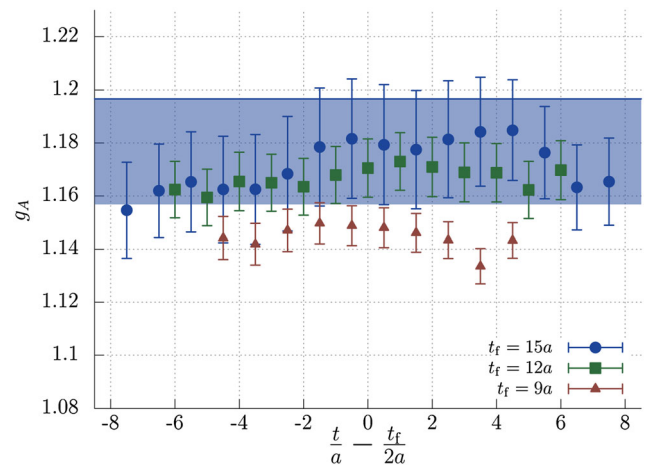


FIG. 4 (color online). The renormalized ratio equation (19) for the example of g_A obtained on ensemble VIII ($m_\pi \approx 150$ MeV, $a \approx 0.071$ fm) for three different values of t_f . The shaded region represents the result of a constant fit in the range $t/a \in [4, 11]$ to the $t_f = 15a$ data.

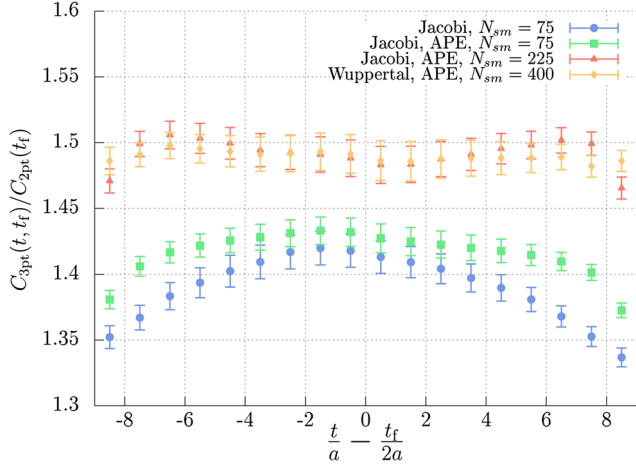


FIG. 5 (color online). The ratio of the three- over the two-point function for g_A at $t_f = 17a$ on ensemble IX ($m_\pi \approx 490$ MeV, $a \approx 0.060$ fm) with different smearing methods.

i.e. increasing the minimal distance between the current and the source-sink δt or reducing the number of t_f values entering the fit. A systematic error was then estimated by varying the fit range, and the parametrization, e.g., allowing for $B_1 \neq 0$ in cases where this parameter was consistent with zero.

In some publications a dependence of the ratio of the axial three-point over the two-point function on t_f and on t is reported that is much stronger than what we observe, see, e.g., Refs. [23,28,36] while the results of, e.g., Ref. [39] are quite similar to ours. This motivates us to compare two different smearing methods found in the literature on ensemble IX: Jacobi smearing [66] and Wuppertal smearing [59]. With the optimized root mean squared smearing radius⁴ $r_{\text{RMS}} \approx 0.58$ fm both methods give similar results, see the comparison between the $N_{\text{sm}} = 225$ Jacobi and the $N_{\text{sm}} = 400$ Wuppertal smearing in Fig. 5. In these cases the parameter B_{01} is statistically compatible with zero. Without realizing additional t_f values we cannot determine B_1 but, based on our detailed investigations on ensembles III, IV and VIII, it is reasonable

⁴All three quarks within the interpolator Φ^\dagger , used to create a state with the quantum numbers of the nucleon, are smeared applying the same matrix A to δ sources. For the case of Wuppertal smearing this matrix A with space and color indices is iteratively defined in Eq. (11). We compute a gauge invariant smearing function $\psi(\mathbf{r}) \geq 0$: $\psi^2(\mathbf{r}) = \sum_{ab} |(A\delta^a)_{r,b}|^2$, where the δ source has only one nonvanishing entry, at the spatial origin and of color a . The RMS radius is computed in the usual way: $r_{\text{RMS}}^2 = [\sum_{\mathbf{n}} r^2 \psi(\mathbf{n}a)] / [\sum_{\mathbf{n}} \psi(\mathbf{n}a)]$, where the sum extends over all (three-dimensional) lattice points and $r^2 = \sum_i \min[(an_i)^2, (an_i - L)^2]$, taking account of the periodic boundary conditions. In principle one could also, by analogy with quantum mechanics, define r_{RMS} with a weight factor $\psi(\mathbf{r})^2$, rather than $\psi(\mathbf{r})$. Due to the approximately Gaussian profile, this definition will result in a radius that is smaller by a factor of about $\sqrt{2}$ than the numbers we quote.

to assume that the effect of this term is statistically insignificant at $t_f = 17a \approx 1.03$ fm.

For the Jacobi algorithm additionally we realize $N_{\text{sm}} = 75$, reducing the smearing radius to $r_{\text{RMS}} \approx 0.37$ fm and $r_{\text{RMS}} \approx 0.34$ fm with and without APE smearing, respectively. This results in some curvature due to the effect of excited states, i.e. the parameter B_{01} now significantly differs from zero. Comparing the two $N_{\text{sm}} = 75$ results illustrates that APE smearing the spatial gauge links is less important than varying the number of smearing iterations. However, APE smearing further increases the overlap with the physical ground state.

For $t_f \rightarrow \infty$ and $t \approx t_f/2$ obviously all four data sets must approach the same asymptotic value. However, from the comparison shown in Fig. 5 it is clear that with the two inferior smearing functions t_f needs to be chosen much larger—or at least additional source-sink distances need to be realized, to enable a determination of the parameters B_1 and B_{01} and a subsequent extrapolation. Otherwise, in these cases an incorrect result would be obtained: Clearly, the minimal sensible value of t_f does not only depend on the statistical accuracy but also on the quality of the interpolator. For instance, an ideal interpolator Φ with 100% ground state overlap would, up to issues related to the locality of the action, eliminate the time dependence altogether.

In Fig. 6 we show data for the renormalized scalar density for the same $m_\pi \approx 150$ MeV ensemble as in Fig. 4. In this case B_{01} significantly differs from zero. We divide

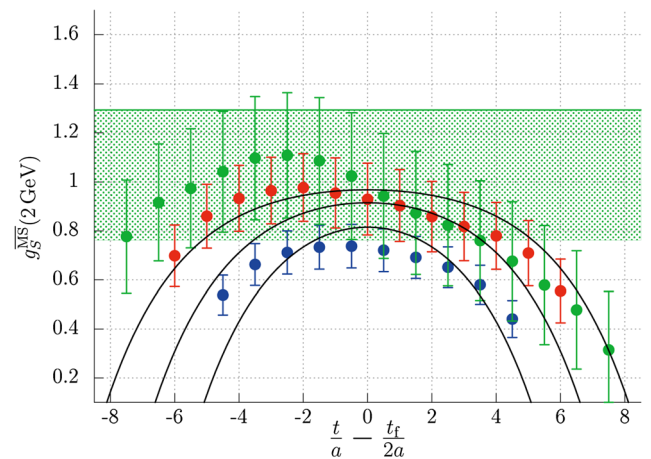


FIG. 6 (color online). The combination $C_{3\text{pt}}(t, t_f)/(A_0 e^{-m_N t})$ with $t_f/a \in \{9, 12, 15\}$ on ensemble VIII ($m_\pi \approx 150$ MeV, $a \approx 0.071$ fm), multiplied by the appropriate renormalization factors to give $\overline{g}_S^{\overline{\text{MS}}}(2 \text{ GeV})$. $A_0 e^{-m_N t}$ corresponds to the ground state contribution to $C_{2\text{pt}}(t_f)$ obtained from a simultaneous fit according to Eqs. (14) and (15) to $C_{3\text{pt}}$ and $C_{2\text{pt}}$. The fit ranges were $t_f/a \in [2, 26]$ for $C_{2\text{pt}}$ and $\delta t = 2a$ for $C_{3\text{pt}}$ where B_1 is set to zero. Also shown are the resulting fit curves for each t_f . The shaded region indicates the fitted value of $\overline{g}_S^{\overline{\text{MS}}}(2 \text{ GeV})$ and the corresponding statistical uncertainty.

the three-point functions by the asymptotic parametrization of the two-point function $A_0 e^{-m_N t}$, obtained from the combined fit. The curves correspond to the multiexponential fit equations (14) and (15) with $\delta t = 2a$. B_1 is compatible with zero. The figure demonstrates that varying t_f helps to obtain a reliable result. However, it is also clear that within statistical errors the $t_f = 15a > 1$ fm data alone would have given the correct value.

Finally, we discuss the tensor charge g_T where the relative errors are—in contrast to g_S —not much bigger than for g_A but excited state contributions are clearly present, as is illustrated in Figs. 7 and 8 for the examples of $m_\pi \approx 150$ MeV and $m_\pi \approx 290$ MeV, respectively. Again, the error bands shown are from multiexponential fits. In Fig. 9 we compare the different smearing methods for the case of g_T . The effect is visible, however, much less dramatic than for g_A (see Fig. 5). In the case of g_T the smearing has only a minor effect on the shape as a function of t but still moves the ratio vertically.

We conclude this section by investigating the lattice spacing dependence of ratios of renormalized three- over two-point functions. This is important as we have only

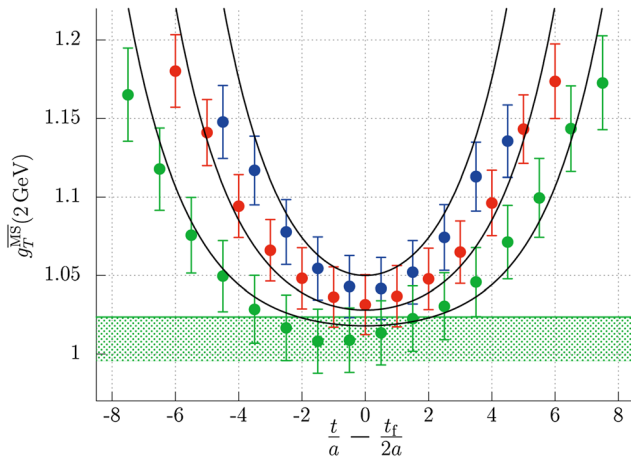


FIG. 7 (color online). The same as Fig. 6 for g_T .

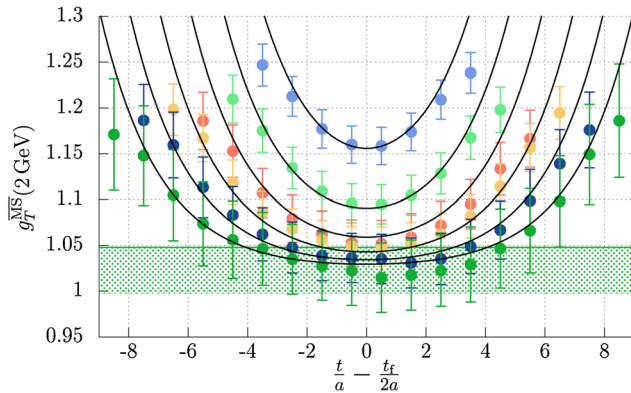


FIG. 8 (color online). The same as Fig. 7 on ensemble IV ($m_\pi \approx 290$ MeV, $a \approx 0.071$ fm) and $t_f/a \in \{7, 9, 11, 13, 15, 17\}$.

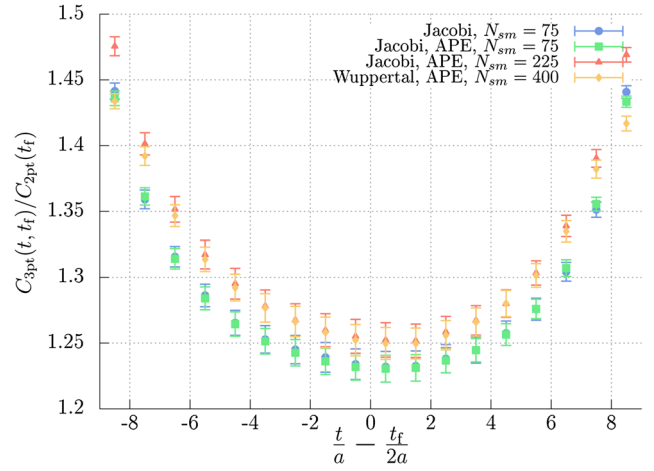


FIG. 9 (color online). The same as Fig. 5 for g_T .

varied t_f on three of our ensembles, albeit at three very different pion masses. From these detailed investigations we concluded that—within the statistics that we have been able to accumulate and with the smearing employed—a single value $t_f \approx 1$ fm was sufficient to obtain the correct ground state results. No lattice spacing effects are visible for effective masses, see Figs. 2 and 3. However, in principle the situation may differ for three-point functions. Therefore, we plot a comparison of the three-point function, normalized with respect to the two-point function for two different pion masses for the couplings with the highest statistical accuracy, g_A and g_T , respectively, in Figs. 10 and 11; no significant dependence of the shape on the lattice spacing can be recognized.

Similar excited state analyses to those detailed above were carried out for all the couplings on all the different ensembles displayed in Table I, also shown in Fig. 1.

C. Comparison with the summation method

The summation method [64] has recently gained in popularity [65]. Fitting ratios in $R(t, t_f)$ to a plateau

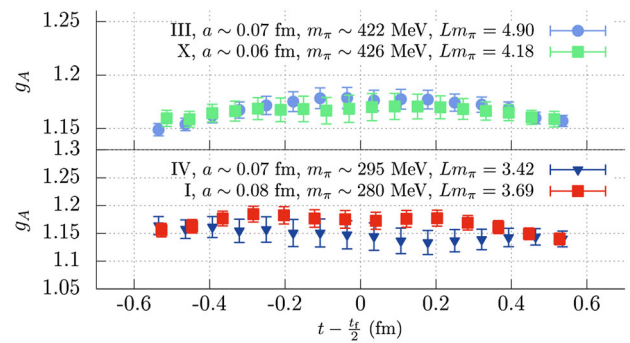
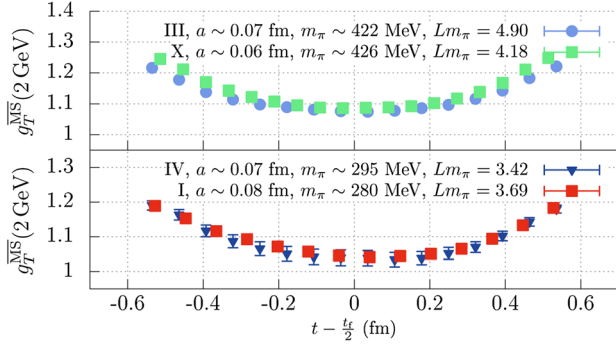


FIG. 10 (color online). Ratios of renormalized three- over two-point functions, giving g_A in the limit $0 \ll t \ll t_f$ for four of our ensembles.

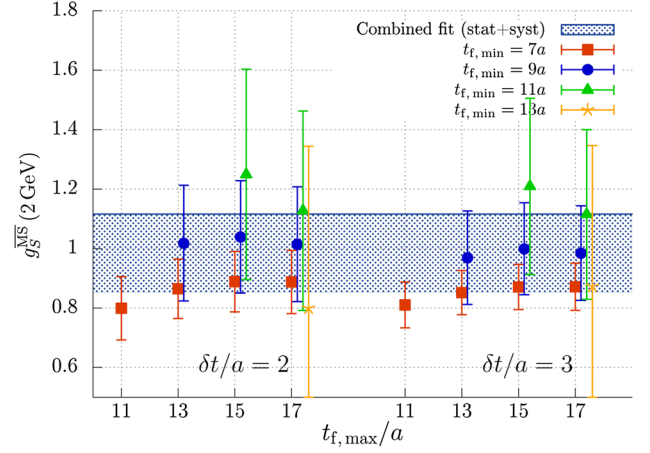
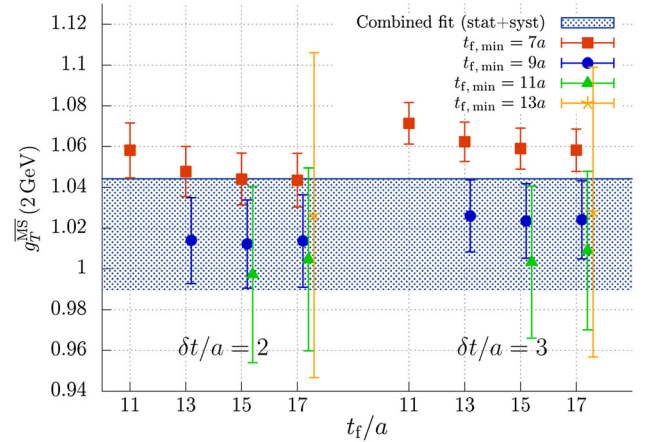

 FIG. 11 (color online). The same as Fig. 10 for $g_T^{\overline{\text{MS}}}(2 \text{ GeV})$.

in t , see Eq. (19), there are corrections of order $\exp(-\Delta m_N t_f/2)$. Instead, the summation method comprises computing sums

$$S(t_f, \delta t) = \sum_{t=\delta t}^{t_f-\delta t} R(t, t_f) = c(\delta t) + \frac{t_f}{a} \left[\frac{\langle N|J|N \rangle}{2m_N} + \dots \right], \quad (21)$$

see Eq. (20), and fitting these linearly in t_f within an interval $t_f \in [t_{f,\min}, t_{f,\max}]$. It is easy to see from Eqs. (14) and (15) that the corrections to the slope, and thereby to the desired matrix element, in this case are only of order $\exp(-\Delta m_N t_f)$. Therefore, for δt chosen sufficiently large and $t_{f,\min} \geq t_{f,\max}/2$, the convergence of the slope as a function of $t_{f,\max}$ towards the asymptotic value is faster than the convergence of results of plateau fits as a function of t_f , at the price of introducing a second fit parameter c . It is not clear why one would compare this procedure to simple plateau fits: In that case, introducing for each t_f value additional fit parameters $c' = B_{01} \exp(-\Delta m_N t_f/2)$ and Δm_N , the leading dependence on $\exp(-\Delta m_N t_f/2)$ can be removed too. If more than one t_f value is available, which is a prerequisite of the summation method, it is also not obvious why one should not attempt the combined fit equations (14) and (15), rather than transforming (and reducing) the available data into sums $S(t_f, \delta t)$.

For g_A , with our interpolator, differences between plateau fits, our combined fit and the summation method cannot be resolved statistically as all $R(t, t_f)$ data for different t_f and $t \approx t_f/2$ basically agree within errors. For examples of these ratios, see Figs. 4 and 10 and the $N_{\text{sm}} = 400$ ratio shown in Fig. 5. In Fig. 12 we compare the result of our combined fit (including a systematic error from varying the fit range and parametrization) to results of the summation method equation (21) for the example of $g_S^{\overline{\text{MS}}}(2 \text{ GeV})$ on ensemble IV. We employ two different minimal distances δt of the summation region in t from the source and sink positions and fit to different intervals $t_f \in [t_{f,\min}, t_{f,\max}]$. Indeed, the summation method converges towards the asymptotic


 FIG. 12 (color online). Results on $g_S^{\overline{\text{MS}}}(2 \text{ GeV})$ obtained with the summation method equation (21) for different fit ranges $t_f \in [t_{f,\min}, t_{f,\max}]$ and $\delta t/a \in \{2, 3\}$ on ensemble IV ($m_\pi \approx 290 \text{ MeV}$, $a \approx 0.071 \text{ fm}$). The error band corresponds to the result obtained with the fit method detailed in Sec. II B, including our assignment of systematic errors. All data are normalized with respect to the $\overline{\text{MS}}$ scheme. The error of the renormalization factor is smaller by more than one order of magnitude than any of the statistical errors displayed and can be neglected.

 FIG. 13 (color online). The same as Fig. 12 for $g_T^{\overline{\text{MS}}}(2 \text{ GeV})$.

result and the convergence rate improves for larger values of $t_{f,\min}$. The same can be seen in Fig. 13 for the tensor coupling $g_T^{\overline{\text{MS}}}(2 \text{ GeV})$.

The form factors $\tilde{g}_T(Q^2)$ and $\tilde{g}_P(Q^2)$ at different virtualities Q^2 show a similar behavior. For the example of the second Mellin moment of the isovector spin-independent structure function $\langle x \rangle_{u-d}$, a comparison between the methods was presented in Ref. [57]. Also in that case we found agreement between the results of the two methods within the respective δt and t_f windows of applicability, however, the combined fits utilize more information than the summation method.

TABLE II. Values of the pion mass, the PCAC lattice quark mass equation (22), the unrenormalized pion decay constant F_π^{lat} and the couplings g_V^{lat} , g_A^{lat} , g_S^{lat} and g_T^{lat} . The errors are statistical and systematic (from varying the fit range and parametrization), respectively.

Ensemble	am_π	$a\tilde{m}$	aF_π^{lat}	g_V^{lat}	g_A^{lat}	g_S^{lat}	g_T^{lat}
I	0.11516(73)(11)	0.003676(38)(10)	0.05056(18)(07)	1.3714(24)(03)	1.566(23)(14)	1.59(17)(05)	1.239(19)(16)
II	0.15449(69)(26)	0.007987(44)(06)	0.04841(43)(05)	1.3461(87)(04)	1.473(31)(04)	1.15(19)(03)	1.275(35)(07)
III	0.15298(43)(16)	0.007964(32)(10)	0.04943(28)(03)	1.3387(17)(01)	1.550(15)(09)	1.35(07)(03)	1.264(14)(11)
IV	0.10675(51)(08)	0.003794(27)(06)	0.04416(37)(05)	1.3539(57)(05)	1.491(30)(02)	1.58(18)(11)	1.188(30)(11)
V	0.10465(37)(08)	0.003734(21)(04)	0.04449(12)(04)	1.3473(30)(05)	1.600(19)(09)	1.49(14)(03)	1.267(20)(05)
VI	0.10487(24)(04)	0.003749(16)(08)	0.04490(12)(04)	1.3445(14)(04)	1.585(17)(05)	1.51(09)(02)	1.221(17)(04)
VII	0.05786(51)(21)	0.001129(18)(04)	0.04048(48)(13)	1.3395(120)(04)	1.521(28)(02)	1.48(38)(05)	1.196(27)(20)
VIII	0.05425(40)(28)	0.000985(17)(08)	0.04029(30)(34)	1.3440(110)(17)	1.540(26)(03)	1.68(28)(13)	1.181(17)(07)
IX	0.15020(53)(06)	0.009323(21)(13)	0.04351(33)(03)	1.3141(15)(02)	1.489(14)(00)	1.57(07)(03)	1.201(22)(10)
X	0.13073(55)(28)	0.007005(23)(04)	0.04152(27)(03)	1.3190(23)(04)	1.492(15)(00)	1.42(10)(01)	1.249(20)(05)
XI	0.07959(25)(09)	0.002633(13)(04)	0.03651(33)(04)	1.3233(50)(06)	1.540(19)(09)	1.51(15)(02)	1.179(17)(18)

III. g_V, g_A AND THE RENORMALIZATION

Following the procedure outlined in Sec. II B, we obtain the unrenormalized values g_A^{lat} , g_S^{lat} , g_P^{lat} and g_T^{lat} listed in Table II. The induced couplings \tilde{g}_T and g_P^* require an extrapolation of nonforward three-point functions in the virtuality Q^2 and will be discussed in detail together with g_S and g_T in Sec. V below. Here we concentrate on g_V and g_A . We also list the pion masses and PCAC lattice quark masses, obtained from the axial Ward identity

$$\tilde{m} = \frac{\partial_4 \langle 0 | A_4 | \pi \rangle}{2 \langle 0 | P | \pi \rangle} [1 + am(b_A - b_P)], \quad (22)$$

where $|\pi\rangle$ is the physical pion state created by an interpolator of spin/flavor structure $(\bar{u}\gamma_5 d)^\dagger$, ∂_μ denotes the symmetrized lattice derivative, $P = \bar{u}\gamma_5 d$ is the local pseudoscalar density and $A_\mu = \bar{u}\gamma_4\gamma_5 d + ac_A\partial_\mu P$ is the nonperturbatively improved axial current (P is automatically order- a improved). c_A was obtained in Ref. [67], the improvement factor $b_A - b_P$ is explained below and m denotes the lattice vector quark mass defined through

$$m = \frac{1}{2a} \left(\frac{1}{\kappa} - \frac{1}{\kappa_{\text{crit}}} \right), \quad (23)$$

where κ_{crit} is the value of the hopping parameter where the PCAC mass vanishes. The lattice quark masses m can easily be computed from the κ values given in Table I and the critical hopping parameter values listed in Table III.

 TABLE III. The critical hopping parameters κ_{crit} , $m = 0$ plaquette values P and renormalization constants [68] of the lattice currents relative to the $\overline{\text{MS}}$ scheme at $\mu = 2$ GeV. The errors given include systematics.

β	κ_{crit}	P	Z_A	Z_V	$Z_S^{\overline{\text{MS}}}(2 \text{ GeV})$	$Z_P^{\overline{\text{MS}}}(2 \text{ GeV})$	$Z_T^{\overline{\text{MS}}}(2 \text{ GeV})$
5.20	0.1360546(39)	0.53861	0.7532(16)	0.7219(47)	0.6196(54)	0.464(12)	0.8356(15)
5.29	0.1364281(12)	0.54988	0.76487(64)	0.7365(48)	0.6153(25)	0.476(13)	0.8530(25)
5.40	0.1366793(11)	0.56250	0.77756(33)	0.7506(43)	0.6117(19)	0.498(09)	0.8715(14)

The PCAC quark masses \tilde{m} (listed in Table II) can be translated into the $\overline{\text{MS}}$ scheme at 2 GeV, upon multiplication with Z_A/Z_P (see below). The pion decay constant is obtained through

$$F_\pi^{\text{lat}} = \frac{\langle 0 | A_4 | \pi \rangle}{\sqrt{2}m_\pi}, \quad (24)$$

where we use the normalization that corresponds to the experimental value $F_\pi = Z_A(1 + amb_A)F_\pi^{\text{lat}} \approx 91$ MeV.

The lattice couplings extracted from the respective matrix elements need to be renormalized too:

$$g_X = Z_X(1 + amb_X)g_X^{\text{lat}}, \quad (25)$$

where $X \in \{S, P, V, A, T\}$. The renormalization factors Z_X and the improvement coefficients b_X depend on the inverse lattice coupling β . No anomalous dimension is encountered for g_V and \tilde{g}_T due to baryon number conservation and for g_A and g_P^* due to the PCAC relation. In the other cases we quote the values in the $\overline{\text{MS}}$ scheme at a scale $\mu = 2$ GeV. As detailed in Ref. [68], the renormalization factors are first determined nonperturbatively in the RI'MOM scheme, using the Roma-Southampton method [69], and then converted perturbatively at three-loop order to the $\overline{\text{MS}}$ scheme. The improvement factors amb_X were computed in Ref. [70] ($X \in \{S, P, V, A\}$) to one loop and confirmed in Refs. [71,72], where b_T is given as well. These are very close to unity, due to the smallness of am , and can be taken into account perturbatively:

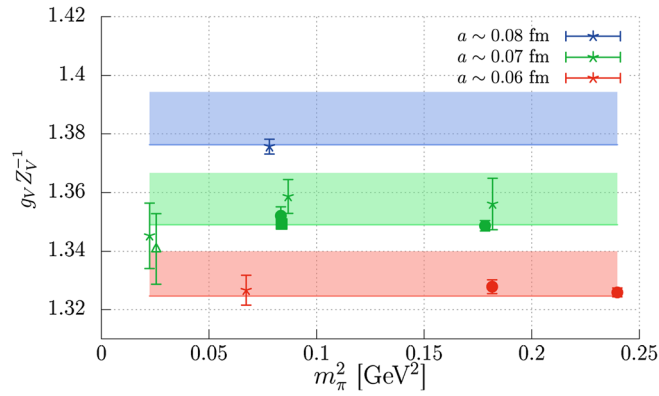


FIG. 14 (color online). $g_V/Z_V \equiv g_V^{\text{lat}}(1 + amb_V)$ as a function of m_π^2 for all ensembles. Symbols are as in Fig. 1. Shown as solid bands are the $1/Z_V$ values determined nonperturbatively [68] (updated in Table III) for the three β values.

$$\begin{aligned}
 b_A &= 1 + 0.15219(5)g^2, & b_V &= 1 + 0.15323(5)g^2, \\
 b_P &= 1 + 0.15312(3)g^2, & b_S &= 1 + 0.19245(5)g^2, \\
 b_T &= 1 + 0.1392(1)g^2. & &
 \end{aligned} \quad (26)$$

In this context we use the “improved” coupling $g^2 \equiv -3 \ln P = 6/\beta + \mathcal{O}(g^4)$, where P denotes the average plaquette with the normalization $P = 1$ at $\beta = \infty$. The corresponding chirally extrapolated values of P are displayed in Table III. Note that $b_m = -b_S/2$ as well as the combination $b_A - b_P \approx 0$ were determined nonperturbatively [73] and for b_S we use the interpolating formula of this reference

$$b_S = (1 + 0.19246g^2) \frac{1 - 0.3737g^{10}}{1 - 0.5181g^4}, \quad (27)$$

instead of the one-loop expression given in Eq. (26).

For convenience we list, in addition to the critical hopping parameter values, the renormalization factors Z_X between the lattice and the $\overline{\text{MS}}$ schemes determined in Ref. [68] (and slightly updated here) in Table III. Note that our Z_A value at $\beta = 5.2$ is by about 2% smaller than that obtained in Ref. [56] from the Schrödinger functional. This is indicative of the $\mathcal{O}(a^2)$ difference between cutoff effects of the two methods. This disagreement indeed reduces with increasing β [74]. Also note that the ratios $Z = Z_P/(Z_S Z_A)$ are consistent with the parametrization obtained from the dependence of the PCAC quark mass on a valence quark hopping parameter by the ALPHA Collaboration [73].

For all ensembles, in Fig. 14 we compare the g_V^{lat} values, multiplied by the improvement terms $[1 + amb_V(\beta)]$, to the corresponding renormalization factors $1/Z_V(\beta)$ of Table III to confirm the relation $g_V = Z_V g_V^{\text{lat}}[1 + amb_V + \mathcal{O}(a^2)]$. We find perfect agreement within errors. The nonperturbative determination of Z_A is very similar to that of Z_V . Therefore, based on this independent validation of $g_V = 1$,

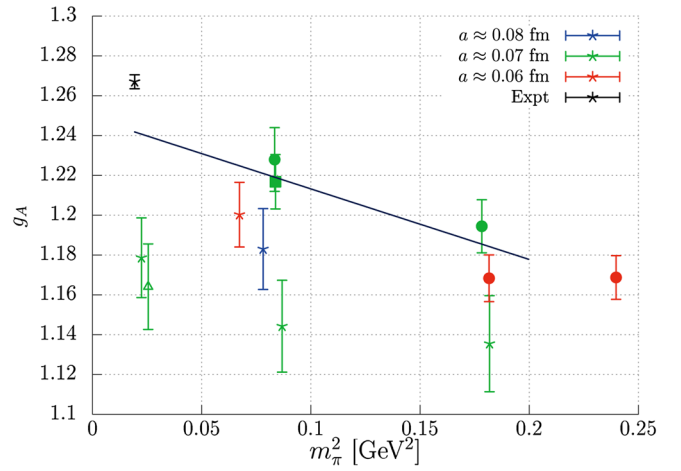


FIG. 15 (color online). g_A as a function of m_π^2 for all ensembles. Symbols are as in Fig. 1: the square corresponds to $Lm_\pi \approx 6.7$, circles to $Lm_\pi > 4.1$, stars to $Lm_\pi \in [3.4, 4.1]$ and the triangle to $Lm_\pi \approx 2.8$. The line drawn to guide the eye represents the result of a linear fit to the four $m_\pi < 430$ MeV points with $Lm_\pi > 4.1$.

we would not expect any problems related to the renormalization of g_A either.

In Fig. 15 we show the renormalized axial coupling as a function of the squared pion mass for all ensembles. The different symbols encode the linear lattice extents Lm_π and the colors the lattice spacings, see Fig. 1. Finite lattice spacing effects cannot be resolved within our errors. Comparing volumes similar in units of m_π , g_A increases with decreasing pion mass. It also increases, enlarging the volume at a fixed pion mass: by about 5% increasing Lm_π from 3.7 to 4.9 at $m_\pi \approx 425$ MeV and by about 6% going from $Lm_\pi \approx 3.4$ to 4.2 at $m_\pi \approx 290$ MeV. When further pushing Lm_π from 4.2 to 6.7, g_A remains constant within a combined error of 1.7%. At the near-physical pion mass the larger volume has an extent $Lm_\pi \approx 3.5$ only, possibly explaining the underestimation of the experimental value by about 7%. Unfortunately, at this pion mass, we do not have a volume with $Lm_\pi > 4.1$ at our disposal which would have required simulating a spatial box of 80^3 points. There is little effect, however, moving from $Lm_\pi \approx 3.5$ down to $Lm_\pi \approx 2.8$. One should not overinterpret this though as it is conceivable that the volume dependence could be small within some range of volumes, due to other effects competing with $N\pi$ and $\Delta\pi$ loop corrections. Naively, one would expect volume effects mediated by pion exchange to be proportional to m_π^2 when keeping the lattice extent fixed in terms of the pion Compton wavelength. Comparing the 290 MeV pion mass points to the 425 MeV points, there is no indication though for the change being larger in the latter case, suggesting a more complex behavior—at least for $Lm_\pi < 4$.

Fitting the $Lm_\pi > 4.1$ values of $g_A(m_\pi^2)$ alone for $m_\pi < 430$ MeV as a linear function of m_π^2 gives the line drawn in Fig. 15, illustrating the remarks made above. The

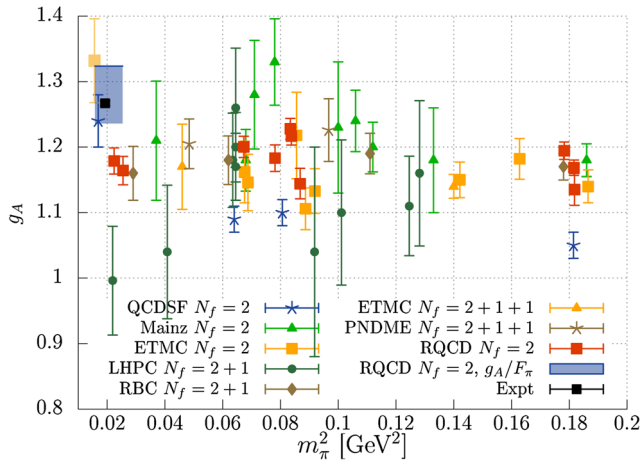


FIG. 16 (color online). g_A as a function of m_π^2 : our results [RQCD, nonperturbatively improved (NPI) Wilson clover] in comparison to other results (fermion action used in brackets). $N_f = 2$: QCDSF [26] (NPI Wilson clover), Mainz⁵ [28] (NPI Wilson clover), ETMC [29] (twisted mass). $N_f = 2 + 1$: LHPC [23] (HEX-smearred Wilson clover), RBC/UKQCD [27] (domain wall). $N_f = 2 + 1 + 1$: ETMC [35] (twisted mass), PNDME [39] (Wilson clover on a HISQ staggered sea). Also indicated as a shaded area is the result from extrapolating our g_A/F_π data to the physical point, see Sec. IV.

line suggests consistency with experiment. At the physical point it reads $g_A = 1.242(15)$, two standard deviations below the known value. However, clearly, with few ensembles at small quark masses and $Lm_\pi > 4$, we cannot at present perform such an extrapolation with any confidence, in particular as the slope is expected to change its sign towards very small pion masses, see, e.g., Ref. [75] as well as Sec. IV below.

Prior to investigating the finite volume behavior in more detail in the next section, in Fig. 16 we put our $N_f = 2$ results on g_A in perspective, comparing these to recent determinations obtained by other collaborations, namely QCDSF [26], the Mainz group⁵ [28] and ETMC [29] for $N_f = 2$, LHPC [23] and RBC/UKQCD [27] for $N_f = 2 + 1$ as well as ETMC [35] and PNDME [39] for $N_f = 2 + 1 + 1$. Most errors displayed are larger than ours, which include the systematics from the renormalization factors, varying fit ranges and parametrizations. This precision is in particular due to our large numbers of measurements and the effort that went into the optimization of the nucleon interpolators. We also indicate in the figure as a shaded area the result of a chiral extrapolation of our data on the ratio g_A/F_π , which we expect to be less affected by finite volume effects, see Sec. IV.

⁵For each of the ensembles studied by the Mainz group two results are given in their article, obtained from plateau fits and from the summation method. We include the summation results since this appears to be their preferred method.

Note that the recent QCDSF study [26] utilizes a smearing different from ours for $m_\pi > 250$ MeV but has significant overlap in terms of the gauge ensembles and the values of Z_A used. These results also carry quite small errors, however, their g_A values are systematically lower, suggesting in these cases that smearing could be an issue, see Fig. 5. The leftmost point of that study, which they associate with $m_\pi \approx 130$ MeV, was obtained using the same smearing that we employ on a subset of ensemble VII [$m_\pi(L) \approx 160$ MeV, $Lm_\pi \approx 2.8$, $m_\pi(\infty) \approx 149.5$ MeV]. Their result at this point (leftmost circle) is compatible within errors not only with experiment but also with our corresponding high statistics result (second red square from the left).

Within errors all recent determinations (with the exception of $m_\pi > 250$ MeV QCDSF results) are consistent with our data. In particular, differences between including the strange or even the charm quark or ignoring these vacuum polarization effects are not obvious. Moreover, in all studies the g_A values appear to be constant or increasing with decreasing pion mass and, where this could be resolved, correlated with the lattice size. In none of the simulations could any significant lattice spacing effects be detected.

IV. FINITE SIZE EFFECTS AND THE AXIAL CHARGE g_A

Above we have seen a noticeable dependence of g_A on the lattice volume for $Lm_\pi < 4.1$. Chiral perturbation theory not only predicts the functional form of the pion mass dependence of hadronic observables but also their finite volume effects, as long as m_π is small enough and $\lambda = Lm_\pi$ sufficiently large. To leading nontrivial order [76,77], the finite size effects on the pion mass read

$$\frac{m_\pi(L) - m_\pi}{m_\pi} = \frac{2}{N_f} h(Lm_\pi, m_\pi), \quad (28)$$

$$h(\lambda, m_\pi) = \frac{m_\pi^2}{16\pi^2 F^2} \sum_{\mathbf{n} \neq 0} \frac{K_1(\lambda|\mathbf{n}|)}{\lambda|\mathbf{n}|}, \quad (29)$$

where F is the pion decay constant in the chiral limit, $m_\pi = m_\pi(\infty)$ is the infinite volume pion mass, $\mathbf{n} \in \mathbb{Z}^3$ are integer component vectors and $K_1(x)$ is the modified Bessel function of the second kind.

The only parameter appearing in Eq. (28), apart from $F = 85.8(6)$ MeV [3,78], is the infinite volume pion mass. Going beyond this order of chiral perturbation theory [79,80], several low energy constants (LECs) are encountered, namely $\tilde{\ell}_i$, $i = 1, 2, 3, 4$ at $\mathcal{O}(p^4)$ and $\tilde{r}_i(m_\rho)$, $i = 1, 2, \dots, 6$ at $\mathcal{O}(p^6)$ (next-to-next-to-leading order, NNLO). We use the parametrization with NNLO chiral perturbation theory input of Ref. [80] to investigate finite volume effects of the pion mass, setting $F = 86$ MeV and using the FLAG

values [78] $\bar{\ell}_3 = 3.41(41)$, $\bar{\ell}_4 = 4.62(22)$ for these two LECs. For $\bar{\ell}_1$, $\bar{\ell}_2$ and \tilde{r}_i we take the central values given in Ref. [81] that were also used in Ref. [80].

We are now in a position to estimate the infinite volume pion masses. We do this by matching the NNLO finite size formula [80] in each case to the pion mass obtained on the largest available volume. Extrapolating this to infinite volume lowers the central value of the pion mass on ensemble III from 422.2 MeV by half a standard deviation to 421.5 MeV, that on ensemble VI (289.5 MeV) by 0.02 MeV and that on ensemble VIII from 149.7 MeV by one sixth of a standard deviation to 149.5 MeV. Having eliminated the free parameter by this matching, we can compare the combination $[m_\pi(L) - m_\pi]/m_\pi^3$ to the leading order chiral expectation $h(\lambda, m_\pi)/m_\pi^2$, see Eqs. (28) and (29), and the NNLO formula of Ref. [80]. This comparison is shown in Fig. 17. Note that we omit the $m_\pi \approx 150$ MeV data from the figure. In this case $[m_\pi(3.42 \text{ fm}) - m_\pi]/m_\pi^3 \approx 3 \text{ GeV}^{-2}$, well off the scale of the figure, while the leading order prediction equation (28) amounts to 0.20 GeV^{-2} and the NNLO prediction [80] to 0.27 GeV^{-2} . On one hand the expansion seems to break down around $Lm_\pi \approx 3.5$ where the differences between the leading order and NNLO curves become large. Already the leftmost point shown in the figure appears to deviate from the predictions. On the other hand, in the safe $Lm_\pi > 4$ region, the exponentially small finite size effects cannot be resolved within the precision of the lattice data.

In Refs. [76,77] the leading order finite size expression of the pion decay constant is given too:

$$\frac{F_\pi(L) - F_\pi}{F_\pi} = -2N_f h(Lm_\pi, m_\pi). \quad (30)$$

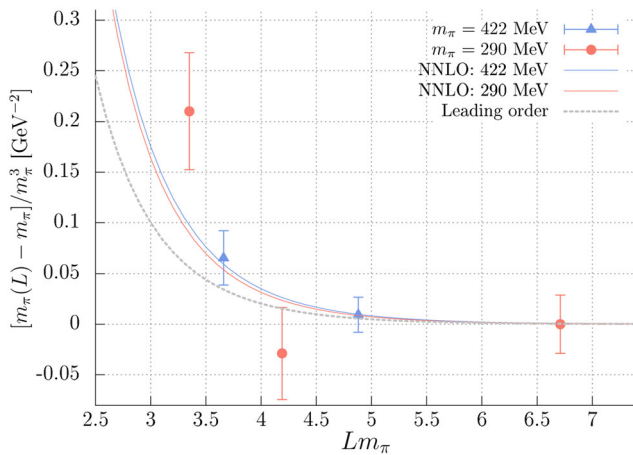


FIG. 17 (color online). The combination $[m_\pi(L) - m_\pi]/m_\pi^3$ as a function of the linear lattice extent, in comparison with the leading order [76] [Eq. (28)] and NNLO [80] chiral perturbation theory expectations.

The leading order finite volume effect of the axial charge in SU(2) chiral perturbation theory contains the same $h(\lambda, m_\pi)$ term [82–84]:

$$\frac{g_A(L) - g_A(\infty)}{g_A^0} = -4h(Lm_\pi, m_\pi) + D(L, m_\pi, \Delta_0), \quad (31)$$

where $g_A^0 = g_A(\infty)$ at $m_\pi = 0$ and we have suppressed the pion mass dependence of $g_A(L)$. The correction $D(L, m_\pi, \Delta_0)$ has been computed taking into account also transitions between the nucleon and the $\Delta(1232)$ resonance in Ref. [84], using the small scale expansion (SSE) technique [85]. Consequently, it depends on the mass difference Δ_0 between the nucleon and the real part of the Δ pole as well as on the squares of the pion-nucleon-nucleon and pion-nucleon- Δ couplings and the ratio of the Δ axial charge over the nucleon axial charge g_1^0/g_A^0 . In the chiral limit the pion-nucleon-nucleon and pion-nucleon- Δ couplings can be reexpressed in terms of g_A^0 , see Eq. (8), and the axial transition charge c_A^0 , respectively. In the SU($2N_f$) quark model $g_1^0/g_A^0 = 9/5$. Note that, although this may not be obvious immediately, the result of Ref. [82] is identical to the expression of Ref. [84] in terms of the volume-dependence equation (31).

In Ref. [26] an approximate cancellation between different contributions to $D(L, m_\pi, \Delta_0)$ over a large range of L and m_π values was observed, which motivated the authors to study the ratio g_A/F_π . From Eqs. (30) and (31) we obtain to leading one-loop order [i.e. $\mathcal{O}(\epsilon^3)$ in the SU(2) SSE [85]]

$$\frac{g_A(L)}{F_\pi(L)} = \frac{g_A(\infty)}{F_\pi} \frac{1 - \frac{g_A^0}{g_A(\infty)} [4h(L) - D(L, \Delta_0)]}{1 - 4h(L)}. \quad (32)$$

For $F_\pi(L)$ also the next-to-leading order and NNLO corrections are known [80], however, to be consistent in terms of the order of the SSE, we do not add these here. We set $g_A^0 = 1.21$ (see below), $c_A^0 = 1.5$ [86], $g_1^0 = 2.2 \approx (9/5)g_A^0$ and $\Delta_0 = 272 \text{ MeV}$ [87]. In Fig. 18 we show the resulting curves for the infinite volume pion masses $m_\pi = 149.5 \text{ MeV}$, $m_\pi = 289.5 \text{ MeV}$ and $m_\pi = 421.5 \text{ MeV}$ as functions of Lm_π . The normalization $g_A(\infty)/F_\pi$ will depend on the pion mass and is adjusted to match the three data sets while the error band is from varying $g_A^0/g_A(\infty) \in [0.9, 1.1]$ within Eq. (32). Indeed, finite volume effects are much reduced, relative to those for g_A visible in Fig. 15, and these are also broadly consistent with the predicted behavior.

Finally, in Fig. 19 we show the ratio $g_A(L)/F_\pi(L)$ as a function of the squared pion mass, together with a linear fit to the $m_\pi < 300 \text{ MeV}$ data, omitting the

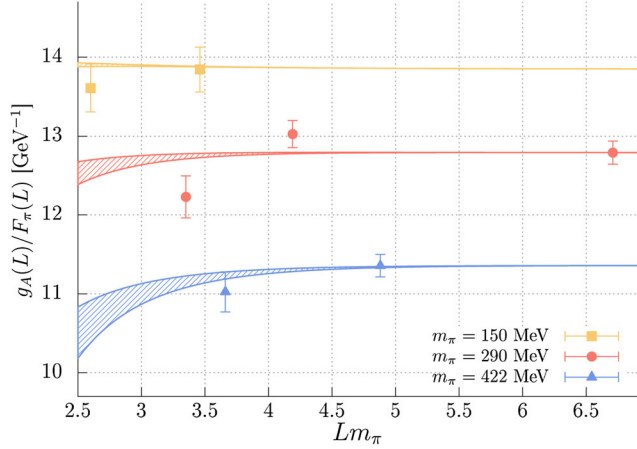


FIG. 18 (color online). The ratio $g_A(L)/F_\pi(L)$ as a function of the linear lattice extent for three different pion masses. The error bands are the predictions of Eq. (32), multiplied by constants $g_A(\infty)/F_\pi$ to match the three data sets. The widths of the error bands are from varying the ratio $g_A^0/g_A(\infty) \in [0.9, 1.1]$.

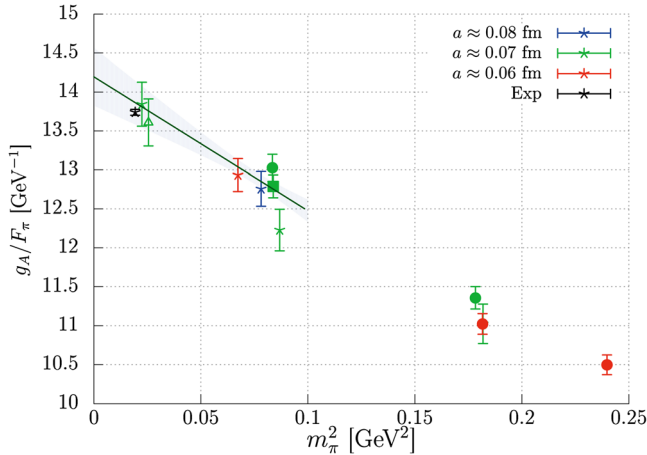


FIG. 19 (color online). g_A/F_π as a function of m_π^2 for all ensembles, together with a linear fit to the low mass points, omitting the smallest volume (ensemble VII). Symbols are as in Fig. 1.

$Lm_\pi < 3.4$ data point (ensemble VII). This fit, with a reduced $\chi^2/N_{\text{DF}} = 5.9/4$, gives $g_A/F_\pi = 13.88(29) \text{ GeV}^{-1}$ at $m_\pi = 135 \text{ MeV}$ which compares well with the experimental result $g_A/F_\pi = 13.797(34)$. Using $F_\pi = 92.21(15) \text{ MeV}$ [3] at the physical point as an input, this gives $g_A = 1.280(27)(35)$, where the second error corresponds to the overall uncertainty of assigning physical values to our lattice spacings [54] (not shown in the figure). We remark that towards the chiral limit g_A decreases with decreasing pion mass while the observed increase of the ratio g_A/F_π is entirely due to an also decreasing pion decay constant. Towards large pion masses F_π will continue to increase while g_A eventually starts decreasing again.

From $F_\pi/F = 1.0744(67)$ [78] we obtain the ratio $g_A/g_A^0 = 1.050(14)$, giving $g_A^0 = 1.211(16)$ using $g_A = 1.2723(23)$ [3]. Using the normalization conventions

$$g_A(m_\pi) = g_A^0 \left(1 + \frac{m_\pi^2}{16\pi^2 F^2} \bar{b} + \dots \right), \quad (33)$$

$$F_\pi = F \left[1 + \frac{m_\pi^2}{16\pi^2 F^2} \bar{\ell}_4 + \dots \right] \quad (34)$$

for the leading chiral corrections, one obtains

$$\frac{g_A(m_\pi)}{F_\pi} = \frac{g_A^0}{F} + \frac{g_A^0}{16\pi^2 F^3} (\bar{b} - \bar{\ell}_4) m_\pi^2 + \dots \quad (35)$$

From our fit we find $\bar{b} - \bar{\ell}_4 = -1.41(36)$ and, using $\bar{\ell}_4 = 4.62(22)$ [78], arrive at the value $\bar{b} = 3.21(42) > 0$ for this LEC: g_A increases with the pion mass [as is also obvious from the ratio $g_A(135 \text{ MeV})/g_A^0 > 1$ above]. Note however that g_A is expected to start decreasing towards larger pion masses, due to the effect of the nearby $\Delta(1232)$ resonance [75,88]. This is also reflected in the lattice data, see Fig. 15.

We did not detect any lattice spacing effects within our statistical errors and therefore so far have ignored these. Not being able to resolve such differences does not mean they are absent and we will readdress this issue in the summary Sec. VI.

V. THE SCALAR, TENSOR AND PSEUDOSCALAR CHARGES

The scalar and tensor couplings can be obtained directly in the forward limit of Eqs. (1) and (5) while the induced tensor and pseudoscalar charges are extracted from extrapolating the respective form factor equations (3) and (4) to small virtualities. We will also determine the value of the induced pseudoscalar form factor $g_p^* = \tilde{g}_p(Q^2)$ at the virtuality $Q^2 = -q^2 = 0.88m_\mu^2 \approx 9.82 \times 10^{-3} \text{ GeV}^2$, corresponding to muon capture [18].

A. The scalar charge g_S

In Fig. 20 we show our results for g_S as a function of m_π^2 . Within their large errors the $m_\pi < 430 \text{ MeV}$ data are consistent with a linear extrapolation and we find no lattice spacing or volume dependence. The result of such an extrapolation to the physical point, fitting the six $m_\pi < 300 \text{ MeV}$ data points with $Lm_\pi > 3.4$ is shown in the figure. We find $g_S^{\overline{\text{MS}}}(2 \text{ GeV}) = 1.02(18)$ for a fit with $\chi^2/N_{\text{DF}} = 0.48/4$.

The charge g_S can, via the conserved vector charge relation, also be obtained as the ratio of the mass splitting

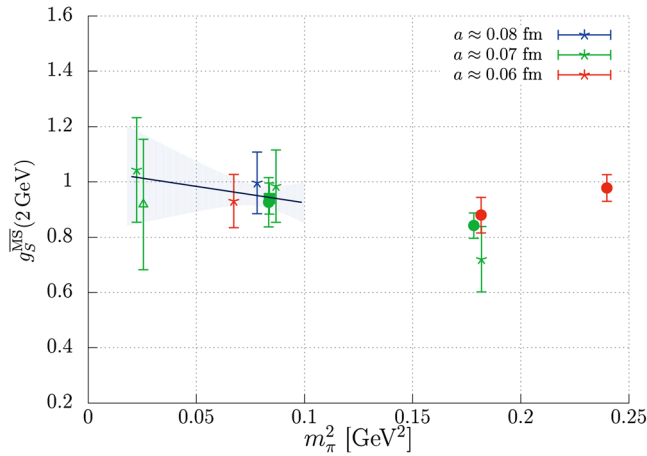


FIG. 20 (color online). $g_S^{\overline{\text{MS}}}(2 \text{ GeV})$ as a function of m_π^2 for all ensembles. Symbols are as in Fig. 1. Also shown is a linear extrapolation in m_π^2 to the physical point.

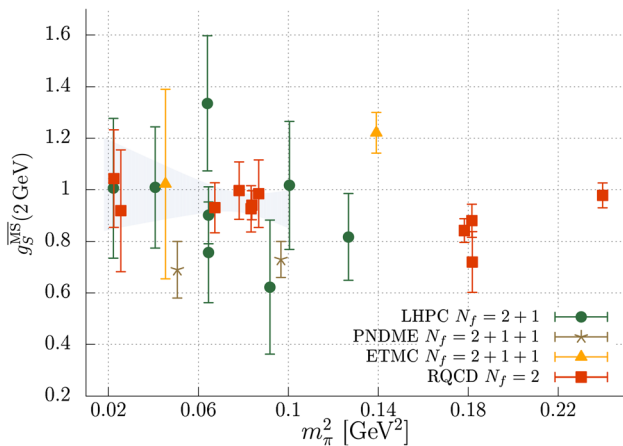


FIG. 21 (color online). $g_S^{\overline{\text{MS}}}(2 \text{ GeV})$ as a function of m_π^2 : our results (RQCD, NPI Wilson clover) in comparison to other results. $N_f = 2 + 1$: LHPC [32] (HEX-smearred Wilson clover). $N_f = 2 + 1 + 1$: PNDME [39] (Wilson clover on a HISQ staggered sea) and ETMC⁶ [40] (twisted mass). Also included is the linear extrapolation of our data points.

of proton and neutron in the absence of electromagnetic interactions over the difference of light quark masses. The determination of this requires either further assumptions or lattice simulations of QCD plus (Q)ED with electrically charged quarks. Recently, such lattice input was used in Ref. [89] to give $g_S = 1.02(11)$. However, not all systematic uncertainties were accounted for in the error estimate. The central value agrees with our direct determination.

In Fig. 21 we compare our results on g_S to recent lattice determinations by other groups, namely LHPC [32], employing $N_f = 2 + 1$ HEX-smearred Wilson-clover fermions, PNDME [39], using clover valence fermions on top of a $N_f = 2 + 1 + 1$ highly improved staggered quark

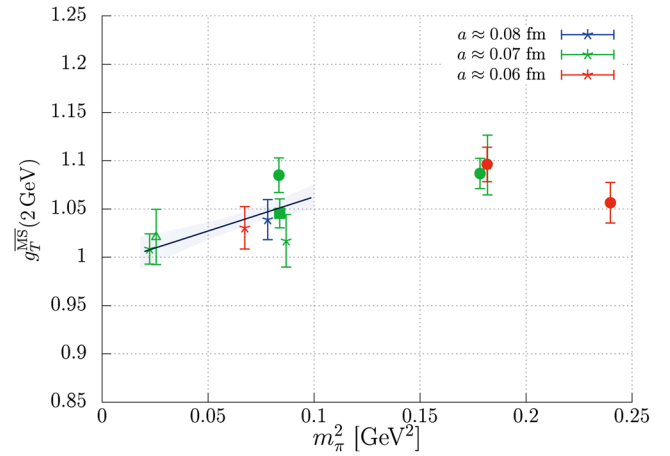


FIG. 22 (color online). $g_T^{\overline{\text{MS}}}(2 \text{ GeV})$ as a function of m_π^2 for all ensembles. Symbols are as in Fig. 1. Also shown is a linear extrapolation in m_π^2 to the physical point.

(HISQ) sea and ETMC⁶ [40], using $N_f = 2 + 1 + 1$ twisted mass fermions. The errors of LHPC are quite large while there appears to be some tension between our results and those of PNDME. Notwithstanding this, around any single pion mass value all results are compatible with each other as well as with our extrapolation on the level of two standard deviations.

B. The tensor charge g_T

In Fig. 22 we show our results on g_T . Again, we cannot detect any lattice spacing or volume effects. Note that for our three $a \approx 0.071$ fm points at $m_\pi \approx 290$ MeV ($m_\pi^2 \approx 0.084 \text{ GeV}^2$), the central value for the largest volume ($Lm_\pi \approx 6.7$) lies in between those for the $Lm_\pi \approx 3.4$ and $Lm_\pi \approx 4.2$ lattices. Again, we show a linear extrapolation to the physical point which gives $g_T^{\overline{\text{MS}}}(2 \text{ GeV}) = 1.005(17)$ with $\chi^2/N_{\text{DF}} = 6.0/4$. Unlike in the case of g_A we regard such an extrapolation of g_T as safe since there are no indications of finite volume effects and our lowest mass point $m_\pi \approx 150$ MeV is already very close to the physical pion mass $m_\pi = 135$ MeV. This conclusion is also supported by Fig. 23 where we compare our results to those of ETMC [31] ($N_f = 2$ twisted mass fermions), RBC/UKQCD [30] ($N_f = 2 + 1$ domain wall fermions), LHPC [32] ($N_f = 2 + 1$ HEX-smearred Wilson-clover fermions), PNDME [39] (Wilson clover on a HISQ staggered $N_f = 2 + 1 + 1$ sea) and ETMC [31] ($N_f = 2 + 1 + 1$ twisted mass fermions). No correlation with the sea quark content, volume, lattice action or lattice spacing is obvious. Moreover, all these determinations are statistically consistent with each other as well as with our extrapolation.

⁶At $m_\pi \approx 370$ MeV we show their $t_f = 14a \approx 1.14$ fm result. In this reference also $N_f = 2$ results at $m_\pi \approx 126$ MeV can be found: 1.01(46) at $t = 12a \approx 1.13$ fm and 1.63(76) at $t = 14a \approx 1.32$ fm.

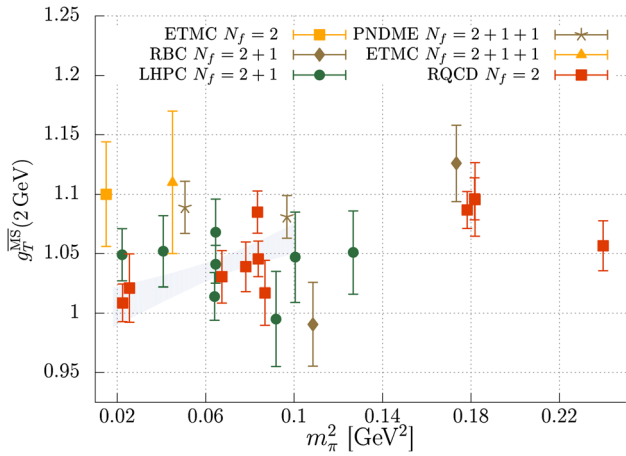


FIG. 23 (color online). $\tilde{g}_T^{\text{MS}}(2 \text{ GeV})$ as a function of m_π^2 : our results (RQCD, NPI Wilson clover) in comparison to other results. $N_f = 2$: ETMC [31] (twisted mass). $N_f = 2 + 1$: RBC/UKQCD [30] (domain wall), LHPC [32] (HEX smeared Wilson clover). $N_f = 2 + 1 + 1$: PNDME [39] (Wilson clover on a HISQ staggered sea), ETMC [31] (twisted mass). Also included is the linear extrapolation of our data.

C. The induced tensor charge \tilde{g}_T

The induced tensor coupling $\tilde{g}_T = \kappa_{u-d} \approx \kappa_p - \kappa_n \approx 3.706$ is well determined experimentally. Computing \tilde{g}_T requires an extrapolation of lattice data obtained at virtualities $Q^2 > 0$ to $Q^2 = 0$. At small Q^2 one can expand

$$g_V(Q^2) = 1 - \frac{r_1^2}{6} Q^2 + \mathcal{O}(Q^4), \quad (36)$$

$$\tilde{g}_T(Q^2) = \tilde{g}_T(0) \left[1 - \frac{r_2^2}{6} Q^2 + \mathcal{O}(Q^4) \right], \quad (37)$$

where the proton isovector Dirac and Pauli radii r_1 and r_2 diverge as the pion mass approaches zero.⁷ It is well known that the Q^2 dependence exhibits a substantial curvature, see, e.g., Refs. [35,38,39,41,42,45,90]. This means small Q^2 values are required for a controlled extrapolation, in particular at small quark masses where the coefficient r_2^2 of the leading Q^2 term becomes large. We expect this effect to partially cancel from the ratio

$$\frac{\tilde{g}_T(Q^2)}{g_V(Q^2)} = \frac{\tilde{g}_T^{\text{lat}}(Q^2)}{g_V^{\text{lat}}(Q^2)} \xrightarrow{Q^2 \rightarrow 0} \tilde{g}_T. \quad (38)$$

Therefore, one of our strategies is to extrapolate this ratio as a linear function of Q^2 to $Q^2 = 0$.

⁷Note that the electric Sachs form factor reads $G_E(Q^2) = g_V(Q^2) - Q^2/(4m_N^2)\tilde{g}_T(Q^2)$. Therefore, in the isospin symmetric limit, the squared charge radius is given as $r_p^2 = r_1^2 + 3\tilde{g}_T/(2m_N^2)$.

Another parametrization that incorporates the curvature is a dipole fit

$$\tilde{g}_T(Q^2) = \frac{\tilde{g}_T(0)}{(1 + Q^2/m_V^2)^2}. \quad (39)$$

Taylor expanding this expression, the linear approximation equation (37) should be valid for $Q^2 \ll m_V^2 \equiv 12/r_2^2$. We show both extrapolations, Eqs. (38) and (39) for our three $m_\pi \approx 290 \text{ MeV}$ volumes (ensembles IV, V and VI, see Fig. 1) in Fig. 24. The \tilde{g}_T/g_V data (shown in the left panel) are compatible with a linear behavior down to our largest $Q^2 \approx 0.6 \text{ GeV}^2 \approx m_\rho^2$ value, however, in this case we restrict ourselves to the range $Q^2 < 0.4 \text{ GeV}^2$ to keep $Q^2 < m_V^2 \approx m_\rho^2$. Note that for $Lm_\pi = 3.4$ only one point lies within this window, so no extrapolation is possible. In the right panel we show the corresponding dipole fits to the $Q^2 < 0.6 \text{ GeV}^2$ data. We see no significant volume dependence between the $Lm_\pi = 3.4, 4.2$ and 6.7 data. Moreover, all five extrapolated values are consistent with each other.

We repeat this procedure for all ensembles and take the central value from dipole fits, adding in quadrature to the statistical error an uncertainty from taking the difference between using the two extrapolation methods and varying the fit range. The resulting induced tensor charges are shown in Fig. 25 as a function of m_π^2 . Due to the different volumes the numbers of points within the fit ranges vary considerably, thus giving rise to significantly fluctuating error sizes. We extrapolate the $m_\pi < 300 \text{ MeV}$, $Lm_\pi > 3.4$ data linearly to the physical point, obtaining $\tilde{g}_T = 3.00(8)$, which is significantly smaller than the experimental value 3.706. While there could be a deviation between this value and the one relevant for the isospin symmetric approximation, one would not expect this to exceed eight of our standard deviations. It is interesting that results obtained at larger pion masses are closer to experiment than our lowest mass point, which dominates the extrapolation. Small volumes result in a larger low-momentum cutoff and a significant loss of precision which complicates resolving the volume dependence. In general, the central values increase with the lattice size and this deserves further study.

In Fig. 26 we compare our results on \tilde{g}_T to recent lattice determinations by other groups, namely QCDSF [42], the Mainz group⁸ [28,46] and ETMC [43] for $N_f = 2$, LHPC [45] and RBC/UKQCD [38] for $N_f = 2 + 1$ as well as ETMC [35] and PNDME [39] for $N_f = 2 + 1 + 1$. With the exception of one LHPC point that carries one of the larger error bars, all the central values are below the experimental result. The figure does not include recent CSSM/QCDSF/UKQCD $N_f = 2 + 1$ stout link NPI Wilson-clover data that, extrapolated to the physical point, give $\tilde{g}_T = 2.8(3)$ [44]. Most points with a precision better

⁸See footnote 5.

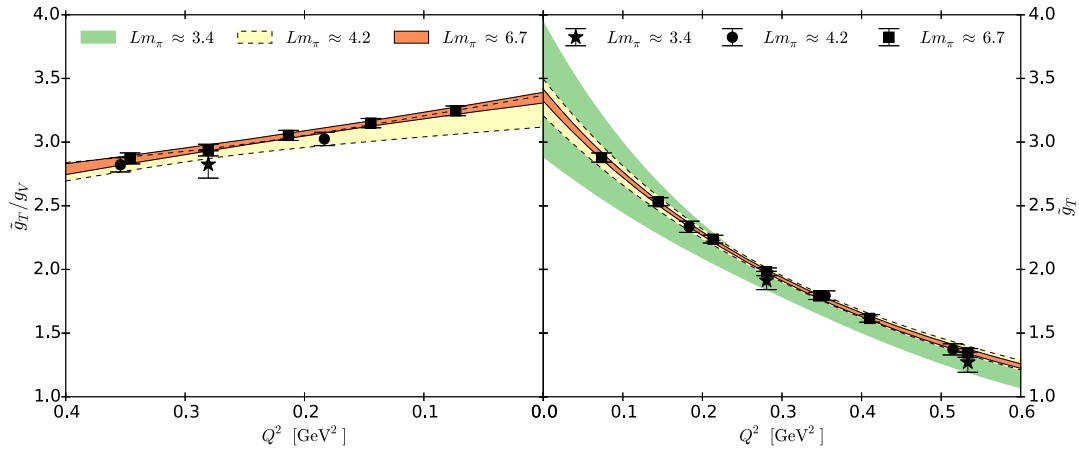


FIG. 24 (color online). $\tilde{g}_T(Q^2)/g_V(Q^2)$ (left panel) and $\tilde{g}_T(Q^2)$ as functions of the virtuality Q^2 at $m_\pi \approx 290$ MeV for three volumes (ensembles IV, V and VI).

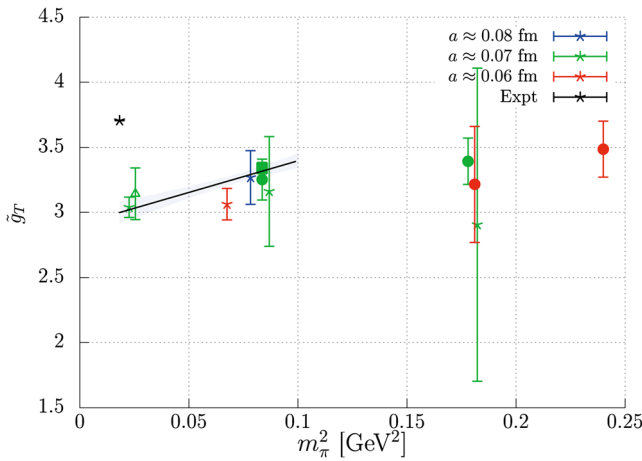


FIG. 25 (color online). The isovector induced tensor charge $\tilde{g}_T = \kappa_{u-d}$ as a function of m_π^2 . Symbols are as in Fig. 1. Also shown is a linear extrapolation in m_π^2 to the physical point.

than 10% are hard to reconcile with the experimental value. At least in part this may be related to finite volume effects that we are not yet able to resolve sufficiently well. Discretization effects will be addressed in Sec. VI.

D. The pseudoscalar couplings g_P^* , $g_{\pi NN}$ and g_P

From Eq. (9) we expect, up to $\mathcal{O}(aQ)$ discretization errors,

$$\frac{\tilde{g}_P(Q^2)}{g_A(Q^2)} = \frac{\tilde{g}_P^{\text{lat}}(Q^2)}{g_A^{\text{lat}}(Q^2)} = \frac{4c_N^2}{m_\pi^2 + Q^2} + \dots, \quad (40)$$

where $c_N \rightarrow m_N$ as $m_\pi \rightarrow 0$ and the ellipses represent corrections due to singularities at $Q^2 < -m_\pi^2$, i.e. terms that are regular at $Q^2 \geq -m_\pi^2$. Pole dominance implies neglecting these terms and setting $c_N = m_N$. In Fig. 27 we test this model assumption by plotting the combination

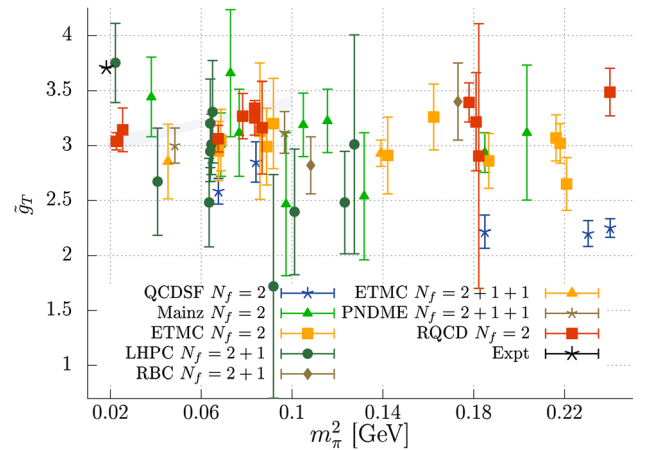


FIG. 26 (color online). The isovector anomalous magnetic moment \tilde{g}_T as a function of m_π^2 : our results (RQCD, NPI Wilson clover) in comparison to other results (fermion action used in brackets). $N_f = 2$: QCDSF [42] (NPI Wilson clover), Mainz⁸ [28,46] (NPI Wilson clover), ETMC [43] (twisted mass). $N_f = 2 + 1$: LHPC [45] (HEX smeared Wilson clover), RBC/UKQCD [38] (domain wall). $N_f = 2 + 1 + 1$: ETMC [35] (twisted mass), PNDME [39] (Wilson clover on a HISQ staggered sea). Also included is the linear extrapolation of our data.

$[\tilde{g}_P(Q^2)/g_A(Q^2)](m_\pi^2 + Q^2)/(4m_N^2)$ as a function of $m_\pi^2 + Q^2$. The data obtained at different pion masses, volumes and lattice spacings appear to follow an almost universal shape, starting out at values around 0.9 at $m_\pi^2 + Q^2 \approx 1$ GeV² and decreasing towards 0.6 for $m_\pi^2 + Q^2 \approx 0.1$ GeV². These deviations of the ratio from unity illustrate that at small virtualities terms other than the contribution of the leading pole cannot be neglected. A similar observation was reported in Refs. [37,38] where for $Q^2 > 0.2$ GeV² and different quark mass values ~ 0.8 were obtained for this ratio. Here, we find deviations from single pole dominance

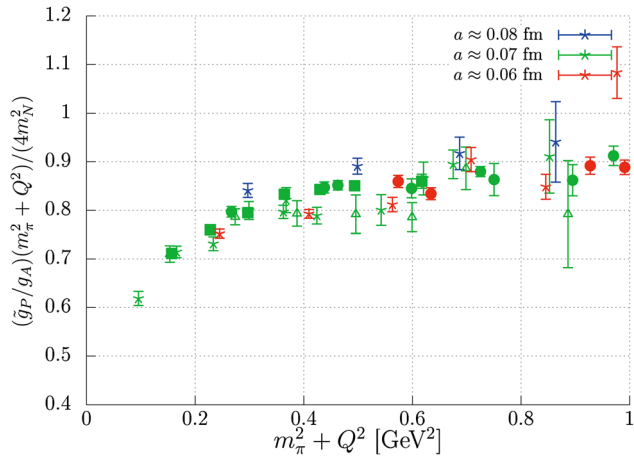


FIG. 27 (color online). The ratio of form factors $\tilde{g}_P(Q^2)/g_A(Q^2)$, normalized with respect to the single pole dominance expectation, as a function of the virtuality Q^2 . Data from all 11 ensembles are plotted on top of each other. Symbols are as in Fig. 1. Deviations from unity quantify violations of the pole dominance model.

to increase towards low momenta, thereby ruling out that a dominant part of these violations can be ascribed to lattice spacing effects.

The induced pseudoscalar coupling for muon capture g_P^* is defined in Eq. (10). It can be obtained, extrapolating the induced pseudoscalar form factor $(m_\mu/m_N)\tilde{g}_P(Q^2)$ to $Q^2 = 9.82 \times 10^{-3} \text{ GeV}^2$. We employ a phenomenological parametrization that incorporates the leading pole:

$$\frac{m_\mu}{m_N} \tilde{g}_P(Q^2) = \frac{c_1}{m_\pi^2 + Q^2} + c_2 + c_3 Q^2, \quad (41)$$

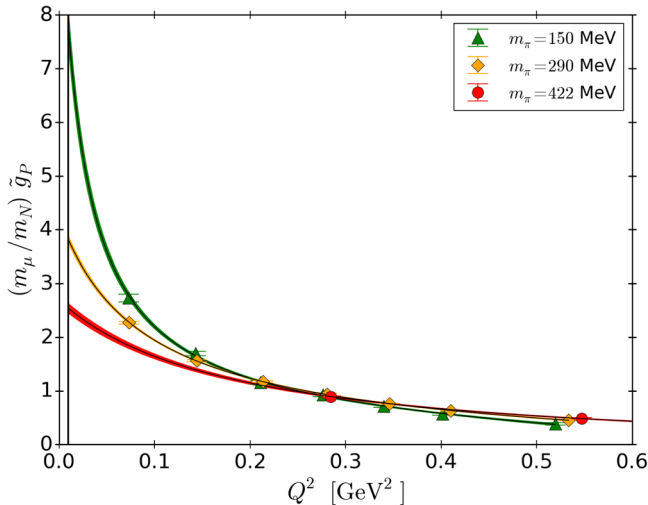


FIG. 28 (color online). Extrapolation of the induced pseudoscalar form factor to the muon capture point $Q^2 = 0.88m_\pi^2$ (vertical line) for three values of the pion mass (ensembles III, VI and VIII). The error bands correspond to fits according to Eq. (41).

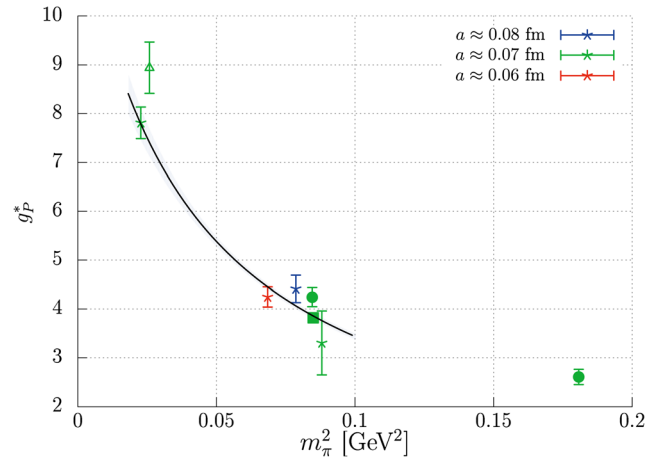


FIG. 29 (color online). Chiral extrapolation of the induced pseudoscalar coupling g_P^* . The error band corresponds to the parametrization equation (42). Symbols are as in Fig. 1.

where the parameters $c_1 < 4m_N^2 g_A^0$, c_2 and c_3 are fitted separately for each ensemble. The terms involving c_2 and c_3 turn out to be necessary to approximate corrections to the pole ansatz, which are regular at positive virtualities.

We display the resulting extrapolations for three pion masses (ensembles III, VI and VIII) in Fig. 28. We are not able to reliably determine the above form factor for $Q^2 > 1 \text{ GeV}^2$ which means results cannot be obtained for the small volume ensembles II, IX and X, where less than four data points are within this range. We show the remaining eight results in Fig. 29 as a function of the squared pion mass. A phenomenological fit of the $m_\pi < 300 \text{ MeV}$, $Lm_\pi > 3.4$ data to the functional form

$$g_P^*(m_\pi^2) = \frac{a_1}{m_\pi^2 + a_2}, \quad (42)$$

with parameters a_1 and a_2 , gives $g_P^* = 8.40(40)$ at the physical point with a $\chi^2/N_{\text{DF}} = 6.4/4$. Since our nearly physical $m_\pi \approx 150 \text{ MeV}$ point dominates the extrapolated value, this is robust against changes of the parametrization. The number obtained compares well with the recent experimental determination of the MuCap Collaboration [91] $g_P^* = 8.06(55)$ and also with the determinations $g_P^* = 8.44(23)$ [18] or $g_P^* = 8.21(9)$ [16] from heavy baryon chiral perturbation theory or $g_P^* = 8.29_{-13}^{+24}(52)$ [92] from covariant baryon chiral perturbation theory. Previously, the RBC and UKQCD collaborations [38] obtained $g_P^* = 6.6(1.0)$, extrapolating $N_f = 2 + 1$ domain wall fermion results to the physical point.

The flavor changing coupling constant $g_{\pi NN}$ between the nucleon and the charged pion is defined as the residue of the pole of the induced pseudoscalar form factor at $Q^2 = -m_\pi^2$:

$$g_{\pi NN} \equiv \lim_{Q^2 \rightarrow -m_\pi^2} \frac{m_\pi^2 + Q^2}{4m_N F_\pi} \tilde{g}_P(Q^2). \quad (43)$$

Implementing the above definition requires an extrapolation of lattice data, which is limited to positive virtualities. Figure 27 demonstrates that corrections to the pole dominance model become significant towards small virtualities. Assuming the parametrization equation (41), we obtain $g_{\pi NN} = c_1/(4m_\mu F_\pi)$, which then needs to be extrapolated to the physical pion mass. However, it is already obvious from Fig. 28 that a controlled extrapolation of $Q^2 \gtrsim 0.1 \text{ GeV}^2$ data to negative virtualities is hardly possible. Indeed, playing around with different parametrizations of $\tilde{g}_P(Q^2)$ that assume a pole at $Q^2 = -m_\pi^2$, values ranging from $g_{\pi NN} \sim 8$ up to $g_{\pi NN} \sim 14$ can easily be produced from our lattice data.

The Goldberger-Treiman relation $g_{\pi NN} \approx m_N g_A / F_\pi$ does not require such an extrapolation, however, it is subject to $\mathcal{O}(m_\pi^2)$ corrections. The relative difference between $g_{\pi NN}$ defined in Eq. (43) and this approximation is known as the Goldberger-Treiman discrepancy

$$\Delta_{\pi N} = \frac{1}{g_{\pi NN}} \left[g_{\pi NN} - m_N \frac{g_A}{F_\pi} \right]_{m_\pi=135 \text{ MeV}}. \quad (44)$$

Using the experimental values of m_N , g_A and F_π , the Goldberger-Treiman relation amounts to $g_{\pi NN} \approx 12.96(3)$ while determinations of $g_{\pi NN}$ from $N\pi$ scattering data result in values $g_{\pi NN} = 14.11(20)$ [93], $g_{\pi NN} = 13.76(8)$ [94] or $g_{\pi NN} = 13.69(19)$ [95]. We remark that obtaining these values also involves extrapolating in Q^2 . Combining the last number quoted above with the Goldberger-Treiman relation translates into $\Delta_{\pi N} = 0.053(13)$. Experimental

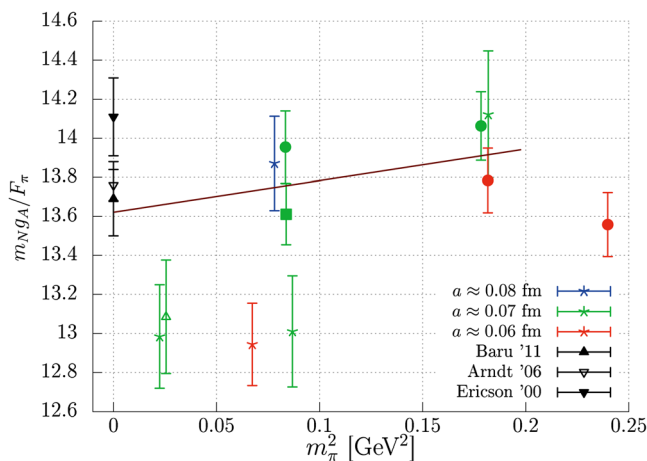


FIG. 30 (color online). The Goldberger-Treiman ratio $m_N g_A / F_\pi$ as a function of the squared pion mass. Symbols are as in Fig. 1. The line indicates a linear extrapolation of $Lm_\pi > 4.1$ data. The experimental values for $g_{\pi NN}$ (black triangles) are from Refs. [93–95].

data, both from nucleon-nucleon scattering and pionic atoms, have been analyzed systematically in the framework of covariant baryon chiral perturbation theory in Ref. [96] (see also references therein), with the central values obtained for $g_{\pi NN}$ ranging from 13.0 to 14.1, depending on the experimental input and the method used (with or without including the Δ resonance).

In Fig. 30 we plot the combination

$$m_N \frac{g_A}{F_\pi} = m_N \frac{g_A^{\text{lat}}}{F_\pi^{\text{lat}}} = g_{\pi NN} [1 + \mathcal{O}(m_\pi^2)] \quad (45)$$

versus m_π^2 , see Eq. (8). As demonstrated in Sec. IV, finite volume effects between g_A and F_π partially cancel, however, the nucleon mass adds a new source of volume dependence. Extrapolating the combination equation (45) to the physical pion mass corresponds to the Goldberger-Treiman approximation while extrapolating it to $m_\pi = 0$ gives the pion-nucleon-nucleon coupling in the chiral limit. A linear fit to the $Lm_\pi > 4.1$ data (indicated as a line) results in $g_{\pi NN}(m_\pi = 0) = 13.62(32)$. This is broadly consistent with the phenomenological values [93–95] that can differ by $\mathcal{O}(m_\pi^2)$ terms. Note, however, that this fit overestimates the known value $m_N g_A / F_\pi = \approx 12.96$ at the physical pion mass by two standard deviations. We conclude that while our results are consistent with expectations, predicting $g_{\pi NN}$ at $m_\pi > 0$ or determining the Goldberger-Treiman discrepancy $\Delta_{\pi N}$ requires different methods, not least due to the significant violations of single pole dominance illustrated in Fig. 27.

Finally, in Fig. 31 we show the pseudoscalar charge, obtained from the first equality in Eq. (8):

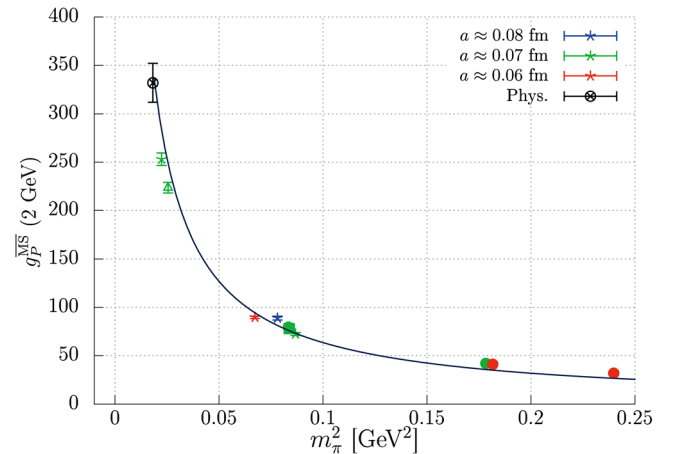


FIG. 31 (color online). The pseudoscalar charge $\overline{g}_P^{\text{MS}}(2 \text{ GeV})$, defined in Eq. (46), as a function of the squared pion mass. Symbols are as in Fig. 1. The physical point (Phys.) is obtained dividing the experimental value of $m_N g_A$ by the $\overline{\text{MS}}$ -scheme quark mass of Ref. [78]. The $1/m_\pi^2$ curve is drawn to guide the eye.

$$g_P^{\overline{\text{MS}}}(2 \text{ GeV}) = Z_P \frac{m_N}{\tilde{m}} g_A^{\text{lat}}(1 + amb_A). \quad (46)$$

Note that order- a improvement is already incorporated into our definition equation (22) of the lattice PCAC mass \tilde{m} , which is why the coefficient b_A rather than b_P appears above. Z_P , κ_{crit} and P [needed to compute amb_A , see Eqs. (23) and (26)] can be found in Table III and g_A^{lat} , the nucleon and lattice PCAC masses in Table II. We expect g_P to diverge like $1/m_{ud}$ and thus, using the Gell-Mann–Oakes–Renner relation, to be proportional to $1/m_\pi^2$. Such a curve is drawn to guide the eye. Using the $N_f = 2$ value $m_{ud}^{\overline{\text{MS}}}(2 \text{ GeV}) = 3.6(2) \text{ MeV}$ of the FLAG Working Group [78], from Eq. (8) we expect $g_P^{\overline{\text{MS}}}(2 \text{ GeV}) = 332(19)$ at the physical point. Our data are broadly consistent with this value: obviously our quark mass, extrapolated to $m_\pi = 135 \text{ MeV}$, is consistent with the FLAG average.

VI. SUMMARY

We have computed all nucleon charges that may be relevant for nonstandard model (and standard model) transitions [6–8] between the neutron and the proton in lattice simulations with $N_f = 2$ mass-degenerate flavors of sea quarks. These isovector couplings are by definition valence quark quantities. Therefore, we do not expect significant effects from including strange (or charm) sea quarks. This claim is substantiated by comparison with lattice results of other groups, some of which have included more sea quark flavors, see Figs. 16, 21, 23 and 26. In contrast to this, the chiral extrapolation may be an issue. Therefore, we have included a point at $m_\pi \approx 150 \text{ MeV}$, close to the physical pion mass. Differences between the numbers obtained at this mass point and our final results, extrapolated to $m_\pi = 135 \text{ MeV}$, were all much smaller than the errors encountered at $m_\pi \approx 150 \text{ MeV}$. This means these extrapolations are under control. Finite volume effects were investigated too and found to be significant in the case of the axial coupling g_A and, by implication, the pseudo-scalar and induced pseudoscalar form factors. These could be much reduced, considering ratios over the pion decay constant F_π , which shares a similar finite volume behavior. Consistency checks were made, regarding the renormalization. The known results for g_V and g_A were reproduced.

The charges, extrapolated to the physical point, as well as g_A in the chiral limit are summarized in Table IV. The first errors displayed contain our statistical and systematic uncertainties related to fit ranges and parametrizations used. The second errors are estimates of the maximally possible discretization effects. These were obtained as follows. To leading order in a , assuming $\mathcal{O}(a^n)$ discretization effects, we can write $g(a) = g(0) + \delta_g a^n / \text{fm}^n = g(0) + \Delta_a g$, where $g(0)$ denotes the continuum limit, $g(a)$ the result for this coupling determined at a fixed lattice spacing and the dimensionless constant δ_g is

TABLE IV. Summary of results, extrapolated to the physical point. The first errors contain statistics and systematics. The second errors are estimates of lattice spacing effects. g_A was obtained, dividing by F_π and therefore a scale setting error is included in the first error that is not subject to further lattice spacing effects. To determine g_A^0 in the chiral limit, the experimental g_A value was used as an input. The experimental g_A and $\tilde{g}_T = \kappa_p - \kappa_n$ numbers are Particle Data Group averages [3] and g_P^* is from the MuCap Collaboration [91].

	Our result	Experiment
g_A	1.280(44)(46)	1.2723(23)
g_A^0	1.211(16)(27)	...
$g_S^{\overline{\text{MS}}}(2 \text{ GeV})$	1.02(18)(30)	...
$g_T^{\overline{\text{MS}}}(2 \text{ GeV})$	1.005(17)(29)	...
\tilde{g}_T	3.00(08)(31)	3.7058901(5)
g_P^*	8.40(40)(159)	8.06(55)

unknown. We varied the lattice constant from $a \approx 0.081 \text{ fm}$ down to $a \approx 0.060 \text{ fm}$. The nondetection of any discretization effect means that our error on a coupling g is bigger than the associated variation: $\Delta g > (0.081^n - 0.060^n) |\delta_g|$. Our extrapolated results are dominated by points at $a = 0.071 \text{ fm}$, meaning that we cannot exclude lattice corrections $\Delta_a g = 0.071^n |\delta_g| < 0.071^n \Delta g / (0.081^n - 0.060^n) \approx 1.7 \Delta g$ ($n = 2$). Therefore, we multiply our errors by this factor. For the induced couplings g^* and \tilde{g}_T the leading discretization effects are linear in a which is why in these cases we allow for discretization errors of $3.7 \Delta g$.

The errors not related to the lattice spacing vary significantly between different couplings. Therefore, our estimates of lattice spacing effects—if obtained as detailed above—become large for some of the channels. However, there is no obvious reason why some couplings should carry much larger discretization effects than others. This means in some cases, in particular for g_S and g_P^* , our discretization error assignment may be overly conservative. However, in the absence of a real continuum limit extrapolation, we do not see any way of reliably estimating this remaining uncertainty.

In addition to the results displayed in Table IV, we find values for the pion-nucleon-nucleon coupling $g_{\pi NN}$, defined in the chiral limit, consistent with experimental estimates, which may not be too surprising, given that g_A comes out correctly. However, violations of the pole dominance model are found to be large, see Fig. 27. We also quote $g_P^{\overline{\text{MS}}}(2 \text{ GeV}) = 332(19)$, which is no independent determination as it relies on the FLAG Working Group quark mass average [78]. Moreover, we determined the low energy constant

$$\bar{b} = 3.21(42), \quad (47)$$

defined in Eq. (33), which encodes the leading order chiral correction to g_A^0 .

The disagreement between the anomalous magnetic moment $\tilde{g}_T = \tilde{g}_T(0)$ and experiment (see Table IV) is puzzling and deserves further attention. The determination of the induced couplings is less direct than computing g_V , g_A , g_S and g_T since it requires extrapolating form factors to vanishing virtuality, where the momentum resolution on a finite volume becomes an issue. The error of this extrapolation to the forward limit reduces with the minimal momentum available π/L while finite volume effects are dominantly functions of the combination Lm_π . Therefore, $Lm_\pi \approx 3.5$ results at $m_\pi \approx 290$ MeV carry much larger errors than at $m_\pi \approx 150$ MeV, which may hide finite volume effects. Moreover, we find excited state contributions to increase with Q^2 . This behavior, while under control at each single value of Q^2 , may become amplified in the slope of the form factor and its extrapolation. We will discuss form factors in detail, including $\tilde{g}_T(Q^2)$, in a forthcoming publication.

While lattice calculations of baryon structure have not yet reached the level of precision of computations of quantities related to meson properties, it is now possible to obtain predictions, e.g., for the isovector scalar and

tensor charges, with uncertainties that have an impact on beyond-the-standard-model phenomenology and in other cases, e.g., for g_P^* , to reduce errors to a level that is competitive with experimental determinations. The next obvious step is to significantly vary the lattice spacing, thus enabling a controlled continuum limit extrapolation, further reducing the remaining uncertainties.

ACKNOWLEDGMENTS

We thank Rajan Gupta and Hartmut Wittig for discussions. The ensembles were generated primarily on the QPACE computer [97,98], which was built as part of the Deutsche Forschungsgemeinschaft SFB/TRR 55 project. The analyses were performed on the iDataCool cluster in Regensburg and the SuperMUC system of the Leibniz Supercomputing Centre in Munich. Additional support was provided by European Union Initial Training Network Grant No. 238353 (ITN STRONGnet) and International Reintegration Grant No. 256594. The BQCD [99] and CHROMA [100] software packages were used extensively along with the locally deflated domain decomposition solver implementation of openQCD [101].

-
- [1] L. M. Brown, *Phys. Today* **31**, No. 9, 27 (1978).
 - [2] C. L. Cowan, F. Reines, F. B. Harrison, H. W. Kruse, and A. D. McGuire, *Science* **124**, 103 (1956).
 - [3] K. A. Olive *et al.* (Particle Data Group), *Chinese Physics C* **38**, 090001 (2014).
 - [4] S. E. Kuhn, J.-P. Chen, and E. Leader, *Prog. Part. Nucl. Phys.* **63**, 1 (2009).
 - [5] M. Ademollo and R. Gatto, *Phys. Rev. Lett.* **13**, 264 (1964).
 - [6] T. Bhattacharya, V. Cirigliano, S. D. Cohen, A. Filipuzzi, M. Gonzalez-Alonso, M. L. Graesser, R. Gupta, and H.-W. Lin, *Phys. Rev. D* **85**, 054512 (2012).
 - [7] A. N. Ivanov, M. Pitschmann, and N. I. Troitskaya, *Phys. Rev. D* **88**, 073002 (2013).
 - [8] V. Cirigliano, S. Gardner, and B. Holstein, *Prog. Part. Nucl. Phys.* **71**, 93 (2013).
 - [9] J. Gasser, M. E. Sainio, and A. Švarc, *Nucl. Phys.* **B307**, 779 (1988).
 - [10] S. Weinberg, *Phys. Rev.* **112**, 1375 (1958).
 - [11] S. L. Adler and F. Gilman, *Phys. Rev.* **152**, 1460 (1966).
 - [12] V. Bernard, L. Elouadrhiri, and U.-G. Meissner, *J. Phys. G* **28**, R1 (2002).
 - [13] T. Fuchs and S. Scherer, *Phys. Rev. C* **68**, 055501 (2003).
 - [14] M. L. Goldberger and S. B. Treiman, *Phys. Rev.* **111**, 354 (1958).
 - [15] V. Bernard, N. Kaiser, and U.-G. Meissner, *Int. J. Mod. Phys. E* **04**, 193 (1995).
 - [16] H. W. Fearing, R. Lewis, N. Mobed, and S. Scherer, *Phys. Rev. D* **56**, 1783 (1997).
 - [17] N. Fettes, U.-G. Meissner, and S. Steininger, *Nucl. Phys.* **A640**, 199 (1998).
 - [18] V. Bernard, N. Kaiser, and U.-G. Meissner, *Phys. Rev. D* **50**, 6899 (1994).
 - [19] V. Bernard, H. W. Fearing, T. R. Hemmert, and U.-G. Meissner, *Nucl. Phys.* **A635**, 121 (1998).
 - [20] H.-W. Lin and S. D. Cohen, Nucleon and pion form factors from $N_f = 2 + 1$ anisotropic lattices, [arXiv:1104.4319](https://arxiv.org/abs/1104.4319).
 - [21] S. Dinter, C. Alexandrou, M. Constantinou, V. Drach, K. Jansen, and D. B. Renner (ETM Collaboration), *Phys. Lett. B* **704**, 89 (2011).
 - [22] S. Capitani, M. Della Morte, G. von Hippel, B. Jäger, A. Jüttner, B. Knippschild, H. B. Meyer, and H. Wittig, *Phys. Rev. D* **86**, 074502 (2012).
 - [23] J. R. Green, M. Engelhardt, S. Krieg, J. W. Negele, A. V. Pochinsky, and S. N. Syritsyn, *Phys. Lett. B* **734**, 290 (2014).
 - [24] M. Lin and S. Ohta (RBC and UKQCD Collaborations), Finite-size scaling in nucleon axial charge from 2 + 1-flavor DWF lattice QCD, *Proc. Sci.*, LATTICE2012 (2012) 171 [[arXiv:1212.3235](https://arxiv.org/abs/1212.3235)].
 - [25] B. J. Owen, J. Dragos, W. Kamleh, D. B. Leinweber, M. S. Mahbub, B. J. Menadue, and J. M. Zanotti, *Phys. Lett. B* **723**, 217 (2013).
 - [26] R. Horsley, Y. Nakamura, A. Nobile, P. E. L. Rakow, G. Schierholz, and J. M. Zanotti, *Phys. Lett. B* **732**, 41 (2014).

- [27] S. Ohta (RBC and UKQCD Collaborations), Nucleon axial charge in $2 + 1$ -flavor dynamical DWF lattice QCD, *Proc. Sci.*, LATTICE2013 (2014) 274 [arXiv:1309.7942].
- [28] B. Jäger, T.D. Rae, S. Capitani, M. Della Morte, D. Djukanovic, G. von Hippel, B. Knippschild, H. B. Meyer, and H. Wittig, A high-statistics study of the nucleon EM form factors, axial charge and quark momentum fraction, *Proc. Sci.*, LATTICE2013 (2014) 272 [arXiv:1311.5804].
- [29] C. Alexandrou, M. Constantinou, V. Drach, K. Jansen, C. Kallidonis, and G. Koutsou (ETM Collaboration), Nucleon generalized form factors with twisted mass fermions, *Proc. Sci.*, LATTICE2013 (2014) 292 [arXiv:1312.2874].
- [30] Y. Aoki, T. Blum, H.-W. Lin, S. Ohta, S. Sasaki, R. Tweedie, J. Zanotti, and T. Yamazaki (RBC and UKQCD Collaborations), *Phys. Rev. D* **82**, 014501 (2010).
- [31] C. Alexandrou, M. Constantinou, K. Jansen, G. Koutsou, and H. Panagopoulos, Nucleon transversity generalized form factors with twisted mass fermions, *Proc. Sci.*, LATTICE2013 (2014) 294 [arXiv:1311.4670].
- [32] J. R. Green, J. W. Negele, A. V. Pochinsky, S. N. Syritsyn, M. Engelhardt, and S. Krieg, *Phys. Rev. D* **86**, 114509 (2012).
- [33] J. D. Bratt *et al.* (LHPC Collaboration), *Phys. Rev. D* **82**, 094502 (2010).
- [34] C. Alexandrou, M. Brinet, J. Carbonell, M. Constantinou, P. A. Harraud, P. Guichon, K. Jansen, T. Korzec, and M. Papinutto (ETM Collaboration), *Phys. Rev. D* **83**, 045010 (2011).
- [35] C. Alexandrou, M. Constantinou, S. Dinter, V. Drach, K. Jansen, C. Kallidonis, and G. Koutsou (ETM Collaboration), *Phys. Rev. D* **88**, 014509 (2013).
- [36] P. M. Junnarkar, S. Capitani, D. Djukanovic, G. von Hippel, J. Hua, B. Jäger, H. B. Meyer, T. D. Rae, and H. Wittig, Nucleon axial form factors from two-flavour lattice QCD, *Proc. Sci.*, LATTICE2014 (2015) 150 [arXiv:1411.5828].
- [37] H.-W. Lin, T. Blum, S. Ohta, S. Sasaki, and T. Yamazaki, *Phys. Rev. D* **78**, 014505 (2008).
- [38] T. Yamazaki, Y. Aoki, T. Blum, H.-W. Lin, S. Ohta, S. Sasaki, R. Tweedie, and J. Zanotti (RBC and UKQCD Collaborations), *Phys. Rev. D* **79**, 114505 (2009).
- [39] T. Bhattacharya, S. D. Cohen, R. Gupta, A. Joseph, H.-W. Lin, and B. Yoon (PNDME Collaboration), *Phys. Rev. D* **89**, 094502 (2014).
- [40] C. Alexandrou, M. Constantinou, K. Hadjiyiannakou, K. Jansen, C. Kallidonis, and G. Koutsou, Nucleon observables and axial charges of other baryons using twisted mass fermions, *Proc. Sci.*, LATTICE2014 (2015) 151 [arXiv:1411.3494].
- [41] S. N. Syritsyn *et al.* (LHPC Collaboration), *Phys. Rev. D* **81**, 034507 (2010).
- [42] S. Collins *et al.* (QCDSF Collaboration), *Phys. Rev. D* **84**, 074507 (2011).
- [43] C. Alexandrou, M. Brinet, J. Carbonell, M. Constantinou, P. A. Harraud, P. Guichon, K. Jansen, T. Korzec, and M. Papinutto (ETM Collaboration), *Phys. Rev. D* **83**, 094502 (2011).
- [44] P. E. Shanahan, A. W. Thomas, R. D. Young, J. M. Zanotti, R. Horsley, Y. Nakamura, D. Pleiter, P. E. L. Rakow, G. Schierholz, and H. Stüben (CSSM and QCDSF/UKQCD Collaborations), *Phys. Rev. D* **89**, 074511 (2014).
- [45] J. R. Green, J. W. Negele, A. V. Pochinsky, S. N. Syritsyn, M. Engelhardt, and S. Krieg, *Phys. Rev. D* **90**, 074507 (2014).
- [46] G. M. von Hippel, S. Capitani, D. Djukanovic, J. Hua, B. Jäger, P. Junnarkar, H. B. Meyer, T. D. Rae, and H. Wittig, Suppression of excited-state effects in lattice determination of nucleon electromagnetic form factors, *Proc. Sci.*, LATTICE2014 (2015) 147 [arXiv:1411.4804].
- [47] S. Syritsyn *et al.*, Initial nucleon structure results with chiral quarks at the physical point, *Proc. Sci.*, LATTICE2014 (2015) 134 [arXiv:1412.3175].
- [48] S. Syritsyn, Review of hadron structure calculations on a lattice, *Proc. Sci.*, LATTICE2013 (2014) 009 [arXiv:1403.4686].
- [49] C. Alexandrou, *AIP Conf. Proc.* **1560**, 3 (2013).
- [50] N. Brambilla *et al.*, *Eur. Phys. J. C* **74**, 2981 (2014).
- [51] M. Constantinou, Hadron structure, *Proc. Sci.*, LATTICE2014 (2015) 001 [arXiv:1411.0078].
- [52] J. Green, Hadron structure from lattice QCD, arXiv:1412.4637.
- [53] G. S. Bali, S. Collins, B. Gläbke, M. Göckeler, J. Najjar, R. H. Rödl, A. Schäfer, R. W. Schiel, and W. Söldner, Moments of structure functions for $N_f = 2$ near the physical point, *Proc. Sci.*, LATTICE2013 (2014) 290 [arXiv:1311.7041].
- [54] G. S. Bali *et al.* (QCDSF Collaboration), *Nucl. Phys.* **B866**, 1 (2013).
- [55] S. Capitani, M. Della Morte, G. von Hippel, B. Knippschild, and H. Wittig, Scale setting via the Ω baryon mass, *Proc. Sci.*, LATTICE2011 (2011) 145 [arXiv:1110.6365].
- [56] P. Fritzsche, F. Knechtli, B. Leder, M. Marinkovic, S. Schaefer, R. Sommer, and F. Virotta (ALPHA Collaboration), *Nucl. Phys.* **B865**, 397 (2012).
- [57] G. S. Bali, S. Collins, B. Gläbke, M. Göckeler, J. Najjar, R. H. Rödl, A. Schäfer, R. W. Schiel, A. Sternbeck, and W. Söldner, *Phys. Rev. D* **90**, 074510 (2014).
- [58] G. S. Bali, H. Neff, T. Düssel, T. Lippert, and K. Schilling (SESAM Collaboration), *Phys. Rev. D* **71**, 114513 (2005).
- [59] S. Güsken, U. Löw, K. H. Mütter, R. Sommer, A. Patel, and K. Schilling, *Phys. Lett. B* **227**, 266 (1989).
- [60] M. Falcioni, M. L. Paciello, G. Parisi, and B. Taglienti, *Nucl. Phys.* **B251**, 624 (1985).
- [61] G. S. Bali, S. Collins, B. Gläbke, M. Göckeler, J. Najjar, R. H. Rödl, A. Schäfer, A. Sternbeck, and W. Söldner, Nucleon structure from stochastic estimators, *Proc. Sci.*, LATTICE2013 (2014) 271 [arXiv:1311.1718].
- [62] R. Evans, G. Bali, and S. Collins, *Phys. Rev. D* **82**, 094501 (2010).
- [63] C. Alexandrou, M. Constantinou, S. Dinter, V. Drach, K. Jansen, K. Hadjiyiannakou, and D. B. Renner (ETM Collaboration), *Eur. Phys. J. C* **74**, 2692 (2014).
- [64] L. Maiani, G. Martinelli, M. L. Paciello, and B. Taglienti, *Nucl. Phys.* **B293**, 420 (1987).
- [65] S. Capitani, B. Knippschild, M. Della Morte, and H. Wittig, Systematic errors in extracting nucleon properties from lattice QCD, *Proc. Sci.*, LATTICE2010 (2010) 147 [arXiv:1011.1358].

- [66] C. R. Allton, C. T. Sachrajda, and C. Michael (UKQCD Collaboration), *Phys. Rev. D* **47**, 5128 (1993).
- [67] M. Della Morte, R. Hoffmann, and R. Sommer (ALPHA Collaboration), *J. High Energy Phys.* 03 (2005) 029.
- [68] M. Göckeler *et al.* (QCDSF and UKQCD Collaborations), *Phys. Rev. D* **82**, 114511 (2010).
- [69] G. Martinelli, C. Pittori, C. T. Sachrajda, M. Testa, and A. Vladikas, *Nucl. Phys.* **B445**, 81 (1995).
- [70] S. Sint and P. Weisz, *Nucl. Phys.* **B502**, 251 (1997).
- [71] Y. Taniguchi and A. Ukawa, *Phys. Rev. D* **58**, 114503 (1998).
- [72] S. Capitani, M. Göckeler, R. Horsley, H. Perlt, P. E. L. Rakow, G. Schierholz, and A. Schiller, *Nucl. Phys.* **B593**, 183 (2001).
- [73] P. Fritzsche, J. Heitger, and N. Tantalo (ALPHA Collaboration), *J. High Energy Phys.* 08 (2010) 074.
- [74] M. Della Morte, R. Sommer, and S. Takeda (ALPHA Collaboration), *Phys. Lett. B* **672**, 407 (2009).
- [75] T. R. Hemmert, M. Procura, and W. Weise, *Phys. Rev. D* **68**, 075009 (2003).
- [76] J. Gasser and H. Leutwyler, *Phys. Lett. B* **184**, 83 (1987).
- [77] J. Gasser and H. Leutwyler, *Nucl. Phys.* **B307**, 763 (1988).
- [78] S. Aoki *et al.* (FLAG Working Group), *Eur. Phys. J. C* **74**, 2890 (2014).
- [79] G. Colangelo and S. Dürr, *Eur. Phys. J. C* **33**, 543 (2004).
- [80] G. Colangelo, S. Dürr, and C. Haefeli, *Nucl. Phys.* **B721**, 136 (2005).
- [81] G. Colangelo, J. Gasser, and H. Leutwyler, *Nucl. Phys.* **B603**, 125 (2001).
- [82] S. R. Beane and M. J. Savage (NPLQCD Collaboration), *Phys. Rev. D* **70**, 074029 (2004).
- [83] M. Procura, B. U. Musch, T. Wollenweber, T. R. Hemmert, and W. Weise, *Phys. Rev. D* **73**, 114510 (2006).
- [84] A. Ali Khan *et al.* (QCDSF Collaboration), *Phys. Rev. D* **74**, 094508 (2006).
- [85] T. R. Hemmert, B. R. Holstein, and J. Kambor, *J. Phys. G* **24**, 1831 (1998).
- [86] T. A. Gail and T. R. Hemmert, *Eur. Phys. J. A* **28**, 91 (2006).
- [87] A. Švarc, M. Hadžimehmedović, H. Osmanović, J. Stahov, L. Tiator, and R. L. Workman, *Phys. Rev. C* **89**, 065208 (2014).
- [88] W. Detmold, W. Melnitchouk, and A. W. Thomas, *Phys. Rev. D* **66**, 054501 (2002).
- [89] M. González-Alonso and J. M. Camalich, *Phys. Rev. Lett.* **112**, 042501 (2014).
- [90] M. Göckeler, T. R. Hemmert, R. Horsley, D. Pleiter, P. E. L. Rakow, A. Schäfer, and G. Schierholz (QCDSF Collaboration), *Phys. Rev. D* **71**, 034508 (2005).
- [91] V. A. Andreev *et al.* (MuCap Collaboration), *Phys. Rev. Lett.* **110**, 012504 (2013).
- [92] M. R. Schindler, T. Fuchs, J. Gegelia, and S. Scherer, *Phys. Rev. C* **75**, 025202 (2007).
- [93] T. E. O. Ericson, B. Loiseau, and A. W. Thomas, *Phys. Rev. C* **66**, 014005 (2002).
- [94] R. A. Arndt, W. J. Briscoe, I. I. Strakovsky, and R. L. Workman, *Phys. Rev. C* **74**, 045205 (2006).
- [95] V. Baru, C. Hanhart, M. Hoferichter, B. Kubis, A. Nogga, and D. R. Philips, *Nucl. Phys.* **A872**, 69 (2011).
- [96] J. M. Alarcón, J. M. Martin Camalich, and J. Oller, *Ann. Phys.* **336**, 413 (2013).
- [97] H. Baier *et al.*, QPACE—A QCD parallel computer based on Cell processors, *Proc. Sci.*, LAT2009 (2009) 001 [arXiv:0911.2174].
- [98] Y. Nakamura, A. Nobile, D. Pleiter, H. Simma, T. Streuer, T. Wettig, and F. Winter, Lattice QCD applications on QPACE, *Procedia Comput. Sci.* **4**, 841 (2011).
- [99] Y. Nakamura and H. Stüben, BQCD—Berlin quantum chromodynamics program, *Proc. Sci.*, LATTICE2010 (2010) 040 [arXiv:1011.0199].
- [100] R. G. Edwards and B. Joó (SciDAC, LHPC, and UKQCD Collaborations), *Nucl. Phys. B, Proc. Suppl.* **140**, 832 (2005).
- [101] See <http://luscher.web.cern.ch/luscher/openQCD/>.